UNIVERSIDADE DE SÃO PAULO
INSTITUTO DE FÍSICA DE SÃO CARLOS

LAUREANO JAVIER ENSUNCHO HERNÁNDEZ

# Indium tin oxide (ITO) and reduced graphene oxide/indium tin oxide (rGO/ITO) thin films: effect of synthesis parameters on ozone gas detection

São Carlos

2021

LAUREANO JAVIER ENSUNCHO HERNÁNDEZ

# Indium tin oxide (ITO) and reduced graphene oxide/indium tin oxide (rGO/ITO) thin films: effect of synthesis parameters on ozone gas detection

Dissertation presented to the Graduate Program in Physics at the Instituto de Física de São Carlos, Universidade de São Paulo to obtain the degree of Master of Science.

Concentration area: Applied physics

Advisor: Prof. Valmor Roberto Mastelaro.

Corrected version

(original version available on the Program Unit)

São Carlos

2021

Ensuncho Hernández, Laureano Javier
Indium tin oxide (ITO) and reduced graphene oxide/indium tin oxide (rGO/ITO) thin films: effect of synthesis parameters on ozone gas detection / Laureano Javier Ensuncho Hernández; advisor Valmor Roberto Mastelaro - corrected version -- São Carlos 2021.
74 p.

Dissertation (Master's degree - Graduate Program in Applied Physics) -- Instituto de Física de São Carlos, Universidade de São Paulo - Brasil , 2021.

1. Gas sensor. 2. Sputtering. 3. Ozone. 4. ITO. 5. Electrical properties. I. Mastelaro, Valmor Roberto, advisor. II. Title.

## ACKNOWLEDGEMENTS

I would first like to express my deep gratitude to my supervisor, Professor Valmor Roberto Mastelaro, who has always shared your knowledge with the project and has always been willing to openly discuss our research directions. I also want to thank you for your patient support and for all of the opportunities that were given to further my research.

My sincere thanks to Brazil and CNPQ for the opportunity to develop my master's degree here. Not all countries so openly receive foreigners and offer such scholarship opportunities.

I want to acknowledge my colleague, Weverton dos Santos Silva, for greatly helping me during my experimental training in the NACA group. Undoubtedly, your help was very important to begin and complete this project.

A very special thanks to Amanda Komorizono, who provided the rGO samples.

I would also like to thank all NACA group members, especially Amanda, Weverton, Gabi, Ramon, Gustavo and Cassio for their loving and kindness during my stay in Brazil.

We would also like to thank the Interdisciplinary Laboratory of Electrochemistry and Ceramics (LIEC-DQ-UFSCar) for the Scanning Electron Microscopy measurements. To the Microfabrication Laboratory (LMF-LNNano) for the structure available to prepare the interdigitated electrodes and for the help of employees Angelo, Maria Helena and Rui (project LMF-14771).

This work was partially supported by Fundação de Amparo à Pesquisa do Estado de São Paulo – FAPESP (Grant n° 2013/07296-2 and 2019/22076-5) and CNPQ (Universal Grant n° 434042/2018-8).

Finally, I am very thankful to my family and my girlfriend for deeply inspiring me to pursue my goals, despite all the difficulties.

*Solo una cosa convierte*
*en impossible un sueño:*
*el miedo al fracasso.*
*Los cuentos de Nasrudin*

## ABSTRACT

ENSUNCHO HERNÁNDEZ, L.J. **Indium tin oxide (ITO) and reduced graphene oxide/ indium tin oxide (rGO/ITO) thin films:** effect of synthesis parameters on ozone gas detection. 2021. 74 p. Dissertation (Master in Science) – Instituto de Física de São Carlos, Universidade de São Paulo, São Carlos, 2021.

Nowadays, continuous attempts are being employed to obtain gas sensors materials with high sensitivity, fast response, good selectivity, and low detection limits. Resistive-based gas sensors based on semiconductor metal oxides (SMOs) are most widely used for gas detection applications. However, their poor selectivity and high operating temperature have given rise to the need to implement several strategies to overcome these drawbacks and, at the same time, reach enhanced sensitivity. Among them, binary, ternary metal oxides, variations in synthesis conditions, and implementing SMOs with other materials, such as reduced graphene oxide (rGO) have been explored. In this context, the gas sensing properties towards ozone gas of Indium Tin Oxide (ITO) thin films obtained by frequency-sputtering method was evaluated. ITO, which is composed of indium oxide ($In_2O_3$) and tin oxide ($SnO_2$)), was deposited under different deposition conditions (ex- and in- situ thermal annealing) and sputtering atmosphere (Ar or Ar+$O_2$), as well as the formation of a rGO/ITO thin film was explored. The results show that the sample heat-treated ex-situ at 300°C presents the best response to ozone gas under the same working temperature and ozone amount. Its optimal operating temperature and thin film thickness towards ozone detection was 300°C and 100 nm, respectively. The film deposited in the argon atmosphere (Ar-film) shows a higher ozone response than that deposited in an argon and oxygen mixing atmosphere (Ar+$O_2$). The rGO/ITO thin film deposited in the Ar atmosphere does not display a larger difference in the response in relation to the ITO film deposited on Ar atmosphere. On the other hand, the rGO/ITO thin films deposited in the Ar and $O_2$ atmospheres (rGO/Ar+$O_2$) exhibit a higher response regarding the ITO film deposited in Ar+$O_2$ atmosphere on the same conditions. Moreover, the ozone sensing response of the rGO/ITO thin film deposited on Ar+$O_2$ atmosphere presents a better response when operating at 200°C. At 200°C, its response is approximately three times compared when measured at 300°C.



Keywords: Gas sensor. Sputtering. Ozone. ITO. Electrical properties.

## RESUMO

ENSUNCHO HERNÁNDEZ, L. J. **Óxido de indio e estanho (ITO) e óxido de grafeno reduzido/ óxido de indio e estanho (rGO/ITO) na forma de filmes finos:** efeito dos parâmetros de síntese na detecção do gás ozônio. 2021. 74 p. Dissertação (Mestrado em Ciências) –Instituto de Física de São Carlos, Universidade de São Paulo, São Carlos, 2021.

Atualmente, diferentes estratégias estão sendo empregadas para obter materiais sensores de gás com alta sensibilidade, resposta rápida, boa seletividade e baixos limites de detecção. Sensores de gás baseados em semicondutores de oxido metálicos (SMOs) resistivos estão entre os mais amplamente usados como aplicações de detecção de gás. No entanto, a maioria dos materiais apresenta baixa seletividade e alta temperatura de operação, senso assim necessário, utilizar diferentes estratégias para superar essas desvantagens e, ao mesmo tempo, atingir maior sensibilidade. Entre eles, o uso de óxidos metálicos binários e ternários, variações nas condições de síntese, bem como a implementação de SMOs com outros materiais, como por exemplo, com o oxido de grafeno reduzido (rGO) tem sido explorados. Nesse contexto, foram avaliadas a propriedades de detecção em relação ao gás ozônio de filmes finos de Óxido de Índio e Estanho (ITO) obtidos pelo método de pulverização catódica por radiofrequência. ITO, que é composto de óxido de índio ($In_2O_3$) e óxido de estanho ($SnO_2$), foi depositado sob diferentes condições de deposição (recozimento térmico ex- e in-situ) e atmosfera de pulverização catódica (Ar ou Ar+$O_2$), bem como a formação de um filme fino de rGO/ITO foi explorado. Os resultados mostram que a amostra tratada termicamente ex-situ a 300°C apresenta a melhor resposta ao ozônio em comparação com os processos ex- e in- situ a 500°C e 200°C, respectivamente, com uma ótima temperatura de operação a 300°C para detecção de ozônio e espessura do filme igual a 100 nm. O filme depositado em atmosfera de argônio (Ar) apresentou uma resposta maior do que o filme tratado em uma atmosfera de argônio e oxigênio (Ar+$O_2$). A formação de um filme de rGO com o filme de Ar (filme rGO/Ar) não levou a uma grande diferença de sensibilidade em relação ao filme de Ar. Por outro lado, o filme depositado sobre rGO e tratado em uma atmosfera de Ar+$O_2$ exibiu uma maior resposta em relação ao filme de Ar+$O_2$. Além disso, a resposta na detecção do ozônio do filme de rGO/Ar+$O_2$ aumentou quando a temperatura operacional foi igual a 200°C. A 200°C, a resposta foi aproximadamente três vezes maior comparada com a medida realizada a 300°C.



Palavras-chave: Sensor de gás. Sputtering. Ozônio. ITO. Propriedades elétricas.

# CONTENTS

# 1 INTRODUCTION

Over the last decades, the concern about atmospheric pollution has been ever-increasing due to significant health problems leding to exposure to gas molecules composing this air pollution. According to the World Health Organization (WHO), air pollution is mainly caused by toxic gases and brought about $7x10^6$ premature deaths in 2012.[1] Additionally, a newly report from the WHO said that over 90% of the world's population living in urban areas are exposed to air pollution levels that exceed WHO guideline limits.[2] Most of these hazardous gases, such as NO, CO, $CO_2$, $NH_3$, $SO_2$, toluene, acetone, ethanol, methanol are routinely and daily released from industrial or agriculture processes, or given off as vehicle exhaust emissions. However, ozone gas, is considered the second most present pollutant in urban areas, and is formed primarily from reactions between two significant classes of air pollutants, $NO_x$ and Volatile Organic Compounds (VOCs), in the presence of ultraviolet radiation (UV).[3] Prolonged exposure to these harmful gases may mount the risk of developing cardiovascular and respiratory diseases, as well as of lung cancer, at levels as low as part-per-million (ppm).[4] Currently, the detection of specific gases resulting from industrial or biological processes is of extreme interest for environmental monitoring, medical diagnosis and control safety. For this purpose, various types of gas sensors have been developed and studied based on different physical and chemical principles.[5–9]

The resistive-based gas sensors are among the most widely applied as gas sensor as, in general, it is simple and easy to fabricate using cost-effective processes. The detection mechanism of such gas sensors is based on the resistance change of a sensing layer upon absorption and reaction in the presence of a specific target gas, which leads to a change in the density of the semiconductor charge carriers, and therefore modifies the material electrical conductivity.[10-11] The sensing materials and the structures of the sensing layer are paramount factors in the gas sensor performance. So, semiconducting metal oxides are among the most potential candidates due to their lower cost, high sensitivity, fast response/recovery time, simple electronic interface, ease of use, low maintenance and ability to detect a large number of gases.[12] The most used semiconducting metal oxides mainly include tin dioxide ($SnO_2$), indium oxide ($In_2O_3$), tungsten dioxide ($WO_3$), zinc dioxide (ZnO), titanium dioxide ($TiO_2$) and also combinations between them have also been frequently reported.[13]

As to the point of view on the sensing mechanism of these materials, many parameters that affect the gas sensor performance such as grain size, the shape of the grains, porosity and the thickness of the gas sensing layer. According to Korotcenkov *et al.*,[14] for most metal oxides, there is no clear description of the relationship between the parameters of sensing materials and sensor performances. Even for the most well-studied metal oxide $SnO_2$, an exhaustive study of its behavior has not yet been accomplished. Additionally, although semiconducting metal oxides present recognized gas sensing properties and appealing simplicity, their poor selectivity and high operating temperature have given rise to the need to implement several strategies to overcome these drawbacks and, at the same time, on the hunt for reaching enhanced sensitivity.[15] Due to which mentioned before, doping of transition metals, noble nanoparticle decoration, functionalization of carbon nanomaterials and graphene/metal oxide semiconductors have been explored.[16]

$In_2O_3$ is a well-known n-type semiconductor that is widely used as a gas sensing material because of its low resistance and easy synthesis.[17] When $In_2O_3$ is doped with $SnO_2$ at relatively high concentrations (around 10% $SnO_2$), it is named indium tin oxide. Indium tin oxide, other than being one of the most widely used transparent conductive oxide, is of great interest when used as a sensing material in the field of gas sensors. Indium tin oxide is used for detecting a wide variety of hazardous gases such as $NO_2$, $NH_3$, $H_2$, CO, ethanol with good sensor responses.[18] For instance, Lee *et al.*,[19] prepared an ITO nanoparticle-based gas sensor, which could detect ppb level of $NO_2$ at 150°C. Xu *et al.*[20] fabricated an ITO nanofibers-based gas sensor toward $NO_2$, the response of which could run 2.4 to 1 ppm at 160°C. On the other hand, the incorporation of reduced graphene oxide with metal oxides or doped metal oxides, paves a new way in gas sensing applications, improving the efficiency of gas sensing material. Indeed, Zhu *et al.* [21] reported a $NO_2$ gas sensor based on rGO/$SnO_2$ nanocomposites, and the sensing response increased three times compared with sensors based on pure rGO. Similarly, Andre *et al.*[22] reported that rGO-$In_2O_3$ composite was as much as 10 times more sensitive than rGO and $In_2O_3$ tested separately regarding $NH_3$ detection.

In this context, we study the gas sensing properties of $In_2O_3$-$SnO_2$ (ITO) compound deposited by the RF magnetron sputtering technique regarding ozone ($O_3$) detection. Moreover, the effect on $O_3$ detection of deposition of ITO on the reduced graphene (rGO) surface (rGO/ITO composite) are also studied.

The background order of this project is presented in the following way: first we present some basic concepts concerning indium tin oxide material. Then, a brief revision about the effect of some synthesis parameters on the structural and microstructural properties of indium tin oxide grown by RF magnetron sputtering technique is detailed. Thirdly, the role of semiconducting metal oxides as sensing materials in the sensor field is presented, followed by a survey of some important papers about indium tin oxide as a gas sensor. Subsequently, a short remark regarding the mixing of semiconducting metal oxides with reduced graphene oxide in the field of gas detection is mentioned and the factors that make ozone detection very important. And finally, the gas detection mechanism of semiconducting metal oxides is presented.

# 2 LITERATURE REVIEW

## 2.1 Indium Tin Oxide compound

Indium tin oxide or tin-doped indium oxide (ITO) is a well-known transparent conductive oxide (TCO). It is a degenerate n-type semiconductor that is composed of indium oxide ($In_2O_3$) and tin oxide ($SnO_2$) with a typical mass ratio of 90:10 [23] and presents a wide band gap of 3.5-4.06 eV.[24] Since ITO films have high transmittance in the visible range of the optical spectrum, high reflectance in the infrared range owing to its high density of free electrons in ITO conduction band and high conductivity similar to a metallic material,[25] they are widely used materials in a variety of electronic and optoelectronic fields, such as panel displays,[26] biological sensors,[27] solar cells,[28] smart windows [29-30] and transparent transistors.[31] ITO has also been the subject of considerable research as chemiresistive gas sensor, and one of the reasons for that is its good linearity and excellent stability against time and temperature variations.[32]

The most common and stable crystal structure of $In_2O_3$ is the bixbyite structure (also known as the c-type rare earth oxide structure, space group $T_h^7$, $Ia\bar{3}$) with a lattice parameter and density of 10.117 $\dot{A}$ and 7.12 $g/cm^3$ [33-34] respectively. This body-centered cubic contains 80 atoms in its cubic unit cell, where 32 atoms correspond to indium atoms and 48 atoms to oxygen atoms. The indium atoms occupy two non-equivalent lattice positions (see Figure 1) surrounded by oxygen atoms, where 8 indium atoms are located in the center of trigonally distorted oxygen octahedrons (b site), while the remanding 24 indium atoms are located in the center of the more distorted octahedrons (d site).[35]

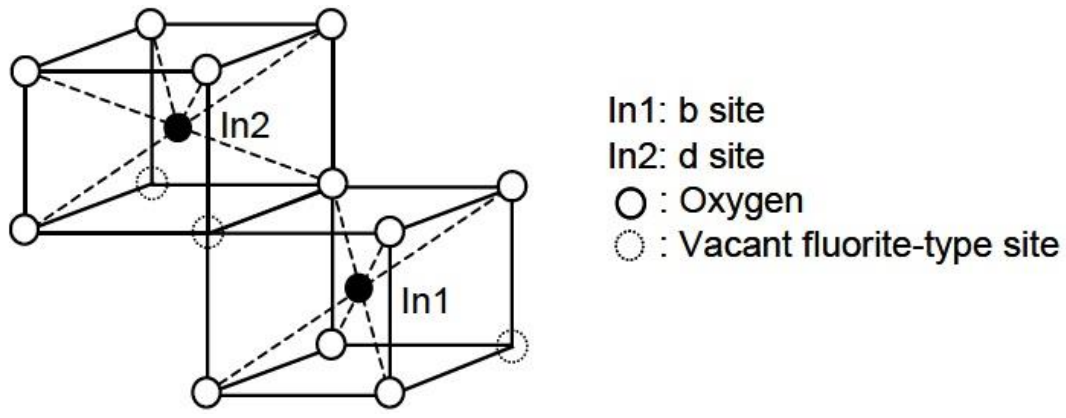


Figure 1 - Different coordination of Indium atoms in $In_2O_3$ crystal.
Source: QIAO.[36]

ITO is essentially formed by replacing the In atoms by Sn atoms in the crystal structure of $In_2O_3$. It was reported that the most preferentially occupied sites by Sn atoms in the cubic bixbyite structure are the less distorted b lattice sites.[35,37]

The high conductivity of ITO has been attributed to both substitutional tin and oxygen vacancies, where the former provides an electron to the conduction band, and the latter contributes at a maximum of two electrons to the electrical conductivity.[38] When this oxide is heavily doped, a phenomenon known as Moss–Burstein shift occurs, that is, the apparent shift of the band gap of the semiconductor towards higher energies, as a result, an optically widening band gap is observed.[39–43]

## 2.2 Factors affecting the ITO properties grown by RF sputtering

ITO thin films are currently obtained using several deposition methods such as physical vapor deposition,[44–47] chemical vapor deposition,[48-49] sol-gel process,[50] spray pyrolysis,[51] etc. Magnetron sputtering is one of the most widely used methods to obtain ITO thin films among these deposition techniques. Compared to other preparation techniques, magnetron sputtering is appropriate for different substrates, a wide range of oxygen partial pressure or temperature conditions, and allows to maintain the stoichiometric ratio of ITO target in the formed films.[52]

The properties of ITO films are quite sensitive to the sputtering deposition conditions such as the sputtering power, deposition atmosphere, substrate temperature, target-to-substrate distance, working pressure, etc. This section considers the effect of sputtering power, deposition atmosphere, and substrate temperature on the ITO properties.

### 2.2.1 Effect of sputtering power: pure Argon (Ar), no substrate heating

In the work of Wu *et al.*[53] where they varied the sputtering power from 15 to 125 W, the crystalline ITO thin films present a preferred orientation change from (222) to (400) as sputtering power increases from 15 to 100 W. However, at 125 W the intensity of the (222) peak is comparable to that of the (400) peak. The lattice constant rises up to 50 W, while for higher sputtering power, it decreases. The decrease of lattice constant was attributed to the reduction of oxygen content at high sputtering power. At surface level, the ITO film deposited

at 125 W has a smoother and denser structure than the 15 W deposited one. Whereas, the work of John *et al.*,[54] who changed sputtering power from 50 to 200 W in steps of 25 W, the ITO thin films are completely amorphous, reaching the crystallization for higher sputtering powers (>100 W). The grain sizes of the crystalline samples are found to increase from 28 to 65 nm as the sputtering power rises from 125 to 200 W.

Kashyout *et al.* [55] studied the crystallization behavior of ITO thin films as a function of annealing and sputtering power varying from 50 to 300 W in steps of 50 W. Similarly, as John *et al.*,[54] they found the as-deposited films are amorphous at low deposition power (50 W). With a slight increase in sputtering power (100 W), it is observed that some planes start to appear dominant at the early growth stage, either the (222) plane or (440) plane, but a preferential crystallization along (400) is generated for higher sputtering powers (>100 W). Post-deposition annealing, the as-deposited films with (400) oriented plane change from (400) to (222) plane. The surface morphology for this as-deposited sample shows columnar grains growing perpendicular to the substrate.

Generally, ITO thin films grown for both low sputtering power and high sputtering power tend to exhibit grains with columnar and compact structure, smooth surface and, grains become larger upon post-deposition annealing.[43,54–57]

### 2.2.2 Effect of deposition atmosphere: without substrate heating

The most commonly used sputtering gases are Ar, $O_2$ and $H_2$, and different combinations during deposition are used to produce ITO films.[58-59] Guillen *et al.* [40] studied the influence of oxygen and annealing atmosphere on the ITO thin films. They observed that the as-deposited ITO layers with various oxygen proportions (0.2, 0.4, 0.8% $O_2$) are amorphous, and crystallization occurs upon annealing at 350°C in a vacuum or air. The annealed ITO films have a (222)-orientated plane. The average roughness values (Ra) and grain size rise when oxygen content is increased (Ra=5, 8, 12 nm), and no significant changes relating to the roughness values are found when ITO films are placed in a vacuum or air atmosphere.

In the work of Marikkannan *et al.*,[58] three different gas combinations (Ar, Ar+$O_2$, Ar+$O_2$+$H_2$) are used during deposition. Among them, the Ar+$O_2$ ambient sputtered ITO film shows the highest root mean square value (Rq=12.9 nm) at the oxygen content of about 5%, while the Ar-only film has an Rq value of 10.9 nm. The as-grown film deposited under pure

Ar ambient crystallizes along the (400) plane, whereas the addition of $Ar+O_2$ changes its preferential orientation along (400) into (222). Similar results about the crystallization of ITO in an oxygen-contained atmosphere are found in Wat *et al.* [59] They reported that the (222) plane is dominant even for lower oxygen percentages. However, some papers reported preferential growth along (440) with oxygen levels similar to the paper mentioned before.[60,61] In all these works, the ITO films show a highly columnar structure.

### 2.2.3 Effect of substrate temperature

Another parameter that significantly affects ITO properties is the substrate temperature. Reddy *et al.*,[62] prepared ITO thin films by varying the substrate temperature from 50 to 400 °C using an RF-power of 50 W. ITO films present a preferred orientation at low substrate temperature (100°C) along (222) plane, but the orientation changes from (222) to (400) with increasing substrate temperature. Additionally, the Rq value decreases with increasing substrate temperature until 300°C and then increases slowly with a further rise in the substrate temperature. The highest and lowest Rq value is found to be 6.76 and 3.10 nm. Similar behavior regarding substrate temperature in Rq value and structural crystallization are found in works even for higher sputtering powers.[63-64]

Significant changes are observed at the surface of ITO film when substrate temperature and sputtering power simultaneously have high values during the deposition process. Yamamoto *et al.*[65] reported ITO nanowires when the substrate temperature is heated at 300°C in an oxygen-free Ar atmosphere and RF power of 300 W. Moreover, they observed that the addition of oxygen (0.73% $O_2$) in the sputtering atmosphere has an inhibitory effect on the growth of ITO nanowires at the same temperature, and therefore, an ITO thin film is formed.

A detailed study of growth parameters influence such as RF-power, oxygen content and substrate temperature on morphology of ITO films is presented by Li et al.[66] The substrate temperature is varied from 100 to 600°C under an RF-power of 250 W and an oxygen flow rate of 0.2 sccm (~0.8% $O_2$). They obtained ITO nanowires at the substrate temperature of 500 °C. Under a fixed RF-power of 250 W and a substrate temperature of 500 °C, they varied the oxygen flow rate (0, 0.2 and 0.4 sccm) during sputtering deposition. ITO nanowires are observed even without oxygen content, however when the oxygen flow rate is

0.4 sccm, an ITO film rather than ITO nanowires is formed. And three different values of sputtering power (200, 250, 300 W) are used with a 0.2 sccm flow rate of oxygen at 500°C. At the power of 200 W, ITO nanorods are grown on the substrate, and ITO nanowires are obtained for 250 and 300 W.

## 2.3 Gas sensor and Semiconducting metal oxides (SMOs)

Even though the human olfactory system is considered the least significant of the human senses,[67] it is highly important, since it warns us about potentially hazardous gases, and is the only active sense during sleep.[68] The human olfactory system can discriminate roughly 400 000 odors.[69] Nevertheless, when the gas concentration is very low or the gas is odorless, it cannot be detected by the human olfactory system. Several types of gases such as $NO_2$, CO, $CO_2$, $O_3$ are harmful to human health when their concentrations are above a critical threshold. Additionally, there are some gases as $H_2$ and $CH_4$ that are explosive when exposed to air. Accordingly, sensitive technological devices are necessary to detect toxic and dangerous gases in our surroundings. In this context, many gas sensors have been developed based on different working principles, such as resistive,[5] optical,[6] ultrasonic and acoustic wave,[7] thermoelectric[8] and electrochemical.[9] Owing to the possibility of detecting both toxic and explosive gases, gas sensors are used in several fields as greenhouse gas monitoring,[70] automotive industry, biomedical applications,[71] and food industry.[72] Figure 2 shows the annual publication in the field of gas sensors during the last five decades, which indicates the ever-increasing demand.

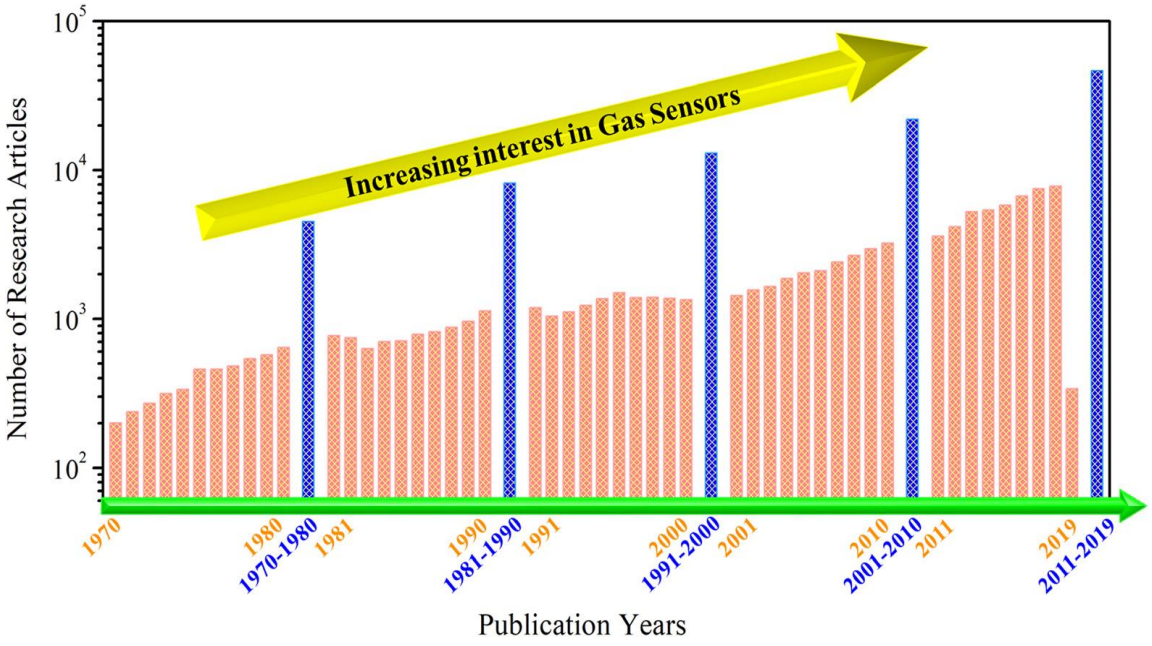


Figure 2 - The annual publication of gas sensors in the last five decades.
Source: MALIK *et al.*[15]

Among these gas sensors, resistive-based gas sensors are most commonly selected for gas sensor device applications[73] and account for more than 20% of the gas sensor market.[74] According to Kim *et al.*,[75] $SnO_2$, ZnO, $TiO_2$, $WO_3$, $In_2O_3$ and $Fe_2O_3$ are the most common sensing materials used as resistive gas sensors. Different combinations between these semiconducting metal oxides have been implemented to improve the sensor parameters, $In_2O_3$-$SnO_2$ (also known as ITO) is one of the most well-known sensing materials in the field of gas sensors.

## 2.4 ITO as gas sensor

There are many reports on ITO-based gas sensors where it has been employed to detect different hazardous gases both reducing and oxidizing, such as $NO_2$, $H_2$, benzene, ethanol, methanol, $NH_3$, CO, formaldehyde, and prepared by various either physical or chemical routes.[76–82] These techniques used for obtaining ITO as a sensing material permit it to present several morphology types as nanorods, nanofibers, nanotubes, nanoparticles and nanowires. Nevertheless, few of these techniques, cited here, thin-film technology is presented. Korotcenkov *et al.*,[83] studied compact $In_2O_3$ and $SnO_2$ films using physical methods of deposition and emphasized that even for smaller thicknesses, they did not have the porosity found in sensors fabricated by other methods. Besides, several experiments have

shown that films grown by sputtering showed an especially dense structure.[84-85] This means that the use of deposition based on physical methods makes films to less gas-permeable.

Although few reports are available on ITO sensors prepared by thin-physical methods, since physical method-prepared thin films as gas sensors have some drawbacks such as low sensitivity and poor selectivity for specific gases,[32] in the literature, one can find specific reports linked to ITO-related gas detection materials obtained by RF magnetron sputtering. Pandya *et al.*,[86] prepared ITO thin films under two different sputtering powers of 200, 300 W (in an Ar-only atmosphere and no substrate heating) and studied their influence on the sensitivity of ITO sensor to ethanol. They found that the ITO film prepared at 200 W following post-deposition annealing at 450°C for 1 h has the highest sensitivity[i] (S=1.14) at 250 °C to 200 ppm ethanol gas. The sputtered ITO film at 200 W shows grains that are much smaller in size and are uniformly distributed. Isik *et al.*,[87] studied the gas sensing properties of ITO thin film regarding two different gases (CO and $H_2$) under the same sputtering conditions. At a fixed sputtering of 300 W and in an oxygen content of 16.3 %, they reported that the sensitivity, response/recovery time is 1.092, 38.9/62.1 s for CO and 1.109, 32.8/36.4 s for $H_2$ at 200 °C.

On the other hand, additional changes in deposition parameters were done by VasanthiPillay *et al.*,[88] to reach an enhanced response to $H_2$. They deposited ITO thin films at 150 W, at the substrate temperature of 375 °C and an oxygen percentage of 60%. The maximum sensitivity is found to be 1.6 at 127°C for 1000 ppm $H_2$. The as-grown film shows a nanoscale system with a non-uniform morphology with bright flower-shaped agglomerates of grains. With the above-aforementioned deposition conditions, VasanthiPillay et al [89,90] studied the effect of annealing on the sensing properties of ITO towards ethanol gas and $NO_2$. The annealed film (427 °C for 1 h) presents higher sensitivity to ethanol than that of the as-deposited one at 377 °C for all ethanol gas concentrations (200-1400 ppm). In particular, at an ethanol gas concentration of 200 ppm, the sensitivity is roughly 40 at 377°C, whereas the maximum sensitivity to 50 ppm $NO_2$ is 28 at 327°C, which is higher than the response of single oxide $SnO_2$, $In_2O_3$ and $Ga_2O_3$, reported in the literature.[91-92] The annealed films show a fine, uniform, and closely packed distribution of polycrystalline nanoclusters free of microcracks.

[i] Sensitivity (S): Ra/Rg (reducing gases) or Rg/Ra (oxidizing gases). Ra and Rg are the electrical resistances under air and test gas respectively.

Zhang *et al.*[93] fabricated ITO materials with different morphologies by adjusting the oxygen content and sputtering power at the substrate temperature of 500 °C. They obtained ITO nanostructures as nanorods and nanowires at 200 and 250 W, when oxygen content is not added during deposition, while ITO films are formed for 0,4 and 0,8 % $O_2$. The sensor made by nanowires was the best one, and the sensitivity of the sensor was 235.6 $mg^{-1}$ at the ethanol gas concentration of 400 ppm under 250°C, and the response and recovery time was 10s and 12s, respectively. The enhanced sensitivity in ITO nanowires is associated with a larger specific area, more oxygen vacancies, and an orientated electron transport channel.

According to the aforementioned statements, Ar gas and sputtering power produce ITO films with a columnar and compact structure that makes films less gas-permeable, which is not good for applications as a gas sensor. Depending on the sputtering parameters, the addition of oxygen during deposition could have good effects on the sensing properties of ITO. On the one hand, the surface roughness increases when oxygen is added without heating the substrate temperature. Surface roughness is directly proportional to the gas sensitivity of the film because more significant roughness results in a larger contact area with the gaseous species. On the other hand, when the substrate temperature is heated, the oxygen content could have either an inhibitory effect or not on the growth of ITO nanostructures. Finally, ITO nanostructures such as nanorods and nanowires emerge with larger surface areas for high RF power and substrate temperature values. ITO sensors with these morphologies have good sensitivity because of their large surface-to-volume ratio.

## 2.5 Reduced graphene oxide (rGO)-SMOs

As mentioned before, the SMOs are the most widely used sensing materials for gas sensor applications but their poor selectivity and high operating temperature have ignited the need to implement several strategies to overcome these drawbacks and, at the same time, reach enhanced sensitivity.[15] An alternative to overcome these limitations is combining SMOs with other materials. Reduced graphene oxide (rGO), synthesized by the reduction of graphene oxide (GO), is a better choice for gas sensing applications because it contains many dangling bonds and defects, resulting in better sensing properties.[68] Andre *et al.*,[22] have reported that rGO-$In_2O_3$ composite is 10 times more sensitive than pure rGO or pure $In_2O_3$ nanofibers regarding the detection of $NH_3$. The combination of $SnO_2$ with rGO increases the

$NO_2$ response at 50 °C by a factor of 3.[94] The work of Na *et al.*,[95] reported that $In_2O_3$-decorated rGO nanosheets exhibit a response of 30 at 120 °C when exposed to 500 ppb $NO_2$, whereas Liu *et al.*[96] produced a flower-like structure that could detect 1000 ppb at 70 °C with a response higher than 1000.

## 2.6 Ozone

Ozone is an allotropic form of oxygen and is one of the most important gases in the stratosphere because of its ability to filter ultraviolet (UV) rays, which is fundamental for the biological balance of the biosphere.[97] Due to its strong oxidizing capacity, it is the primary disinfectant used worldwide.[98] On the other hand, when its level exceeds a specific threshold value (higher than 120 ppb (daily exposure), in accordance with the European Guidelines), exposure to this gas becomes hazardous to human health since it causes a headache, burning eyes, respiratory irritation, and lung damage.[99] The ground-level ozone forms upon interactions of nitrogen oxides ($NO_x$) and Volatile Organic Compounds (VOCs) with UV radiation and is considered as the second most present pollutant in urban areas.[3] Thus, these factors make the detection of ozone very important.

## 2.7 Gas sensing mechanism of SMOs

In any SMO (n- or p-type) with gas sensing properties, its mechanism is mainly based on a change in electrical conductivity or resistivity after they are exposed to the target gases. This change is related to the chemical interaction between ionosorbed surface oxygen and target gas type on the surface material.[10-11] The adsorbed oxygen molecules on the surface can trap free electrons from the conduction band of the semiconductor, which results in the formation of negatively charged oxygen ions, including $O_2^-$, $O^-$ and $O^{2-}$ at different operating temperatures.[100-102] Below a temperature $147\ °C$, oxygen is ionosorbed as $O_2^-$ and it is ionosorbed as $O^-$, when the working temperature is increased between $147\ °C$ and $397\ °C$, which is usually the operating temperature range of the gas sensors. And over $397\ °C$ formation of $O^{2-}$ occurs.[102] The presence of charged species on the surface of a semiconductor induces a band bending and formation of a depletion layer.[103] The depletion layer is also known as the space-charge layer or electron-depleted region.

The conductivity of the gas sensor relies on both the semiconductor type and the target gases. When the gas sensor is exposed to reducing or oxidizing gases, this will affect the density of charge carriers (n-type electrons or p-type holes) in the near-surface region of each grain. Reducing gases will remove the surface-bound oxygen atoms, allowing the transfer of the negative charge (trapped electrons) to the semiconductor, decreasing the space-charge thickness and, at the same time, the potential barrier between grains (upper-right side). On the other hand, oxidizing gases will interact with the trapped electrons by the oxygen molecules on the surface of SMO, generating that other electrons are extracted from the conduction band, and therefore increasing the space-charge region as well as the potential barrier (lower-right side). Thus, the target gas molecules will decrease or increase the charge carriers, which leads to a change in the materials' conductance.[104–106]

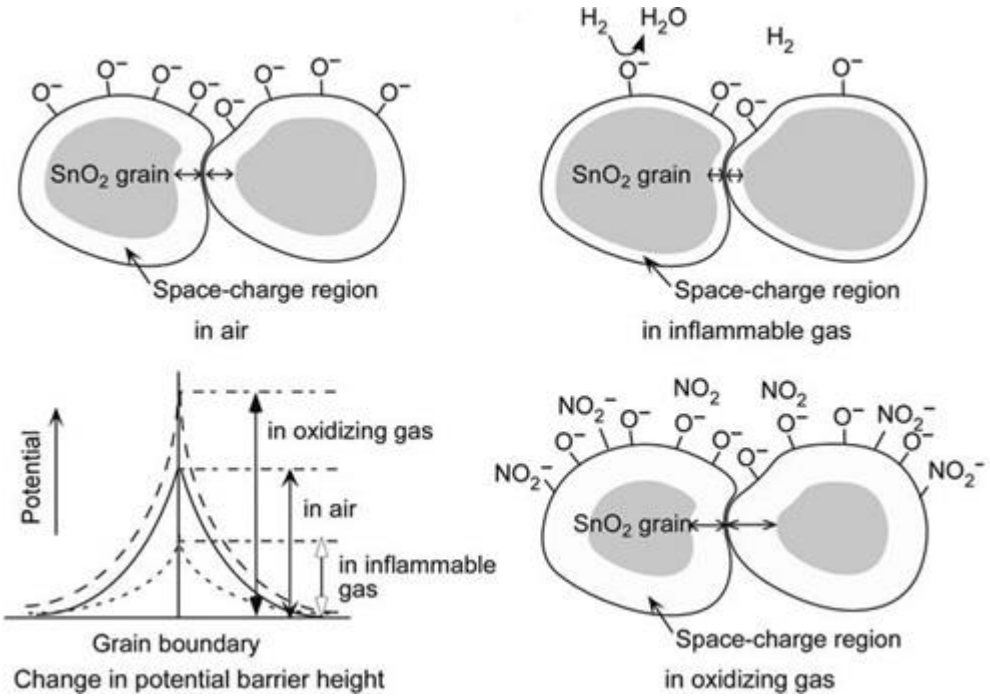


Figure 3 - Detection mechanism of a n-type SMO when exposed to reducing gas $H_2$ (upper-right side) and oxidizing gas $NO_2$ (lower-right side) .
Source: SHIMIZU. [107]

Table 1 shows the behavior of resistance by changing gas atmosphere for n-type and p-type semiconductors:

Table 1 - Resistance behavior according to the exposed gas.

| *Classification* | *Reducing gas* | *Oxidizing gas* |
|---|---|---|
| *n-type* | Resistance decrease | Resistance increase |
| *p-type* | Resistance increase | Resistance decrease |

Source: DEY. [102]

## 2.8 Conduction process in thin films

As mentioned before, when oxygen molecules are adsorbed at the semiconductor metal oxide surface, at the same time, an electron depleted region and upward band bending are generated (see Figure 4), where this latter forms a potential barrier at the grain boundary (also known as Schottky barrier). This electron-depleted region and inter-grain connection are responsible for becoming the gas absorption into a measurable electrical signal. According to the conduction and response models for metal oxide gas sensors[108–110] the conductivity of a grain network is confined by the resistance of inter-grain contacts. In contrast the interaction between gaseous species and the surface of the semiconductor metal oxide is controlled by the surface energetics and the area accessible for absorption.

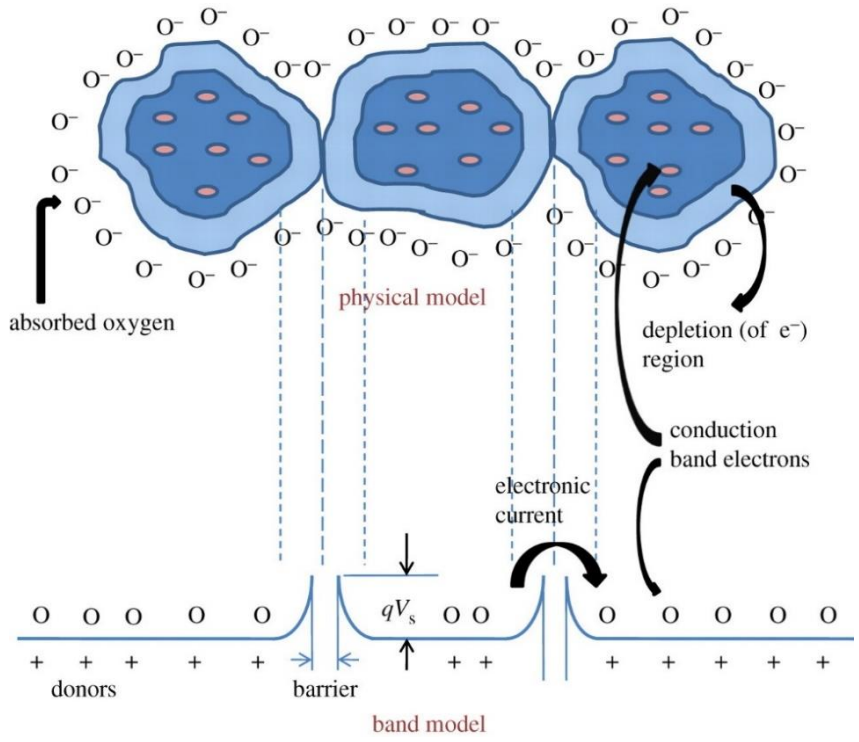


Figure 4 - Energy band model for a semiconductor metal oxide. Three grains showed how the inter-grain contact resistance occurs. The height of the energy barrier is $qV_s$.
Source: SHARMA *et al.*[111]

The gas-sensing performance can take place at different sites of the sensing layer, depending on its morphology. The thin film morphology can be divided into compact and porous ones.[108] For the former, gases cannot penetrate into the layer, and the gas sensing reaction is only confined to the surface of the sensing layer. In the latter approach, gases can access the whole volume of the sensing layer, and the gas sensing reaction can take place both

at the surface of individual grains and at grain-grain boundaries. Figure 5, shows the gas interaction for the two ways stated before.

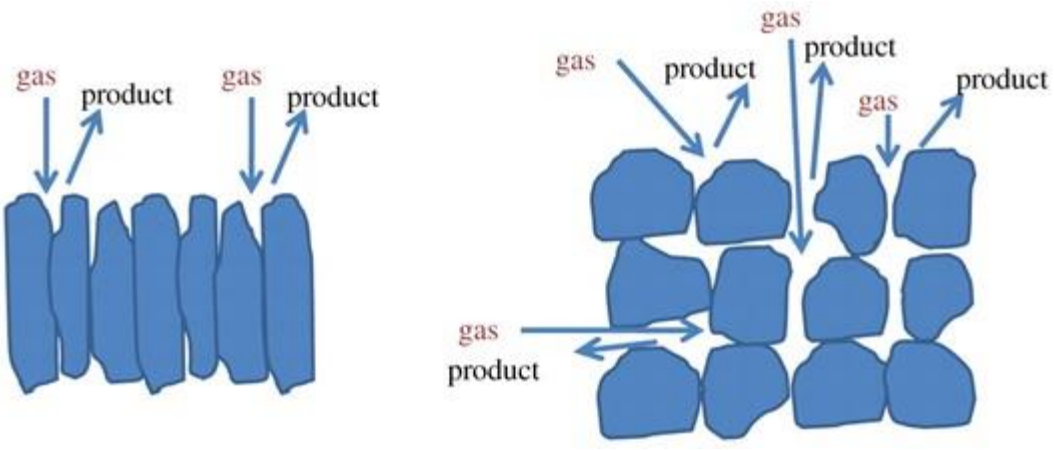


Figure 5 - Schematic of gas sensing interaction in (left) compact layer and (right) porous layer.
Source: SHARMA *et al.*[111]

At the intergranular contact, two space charge layers back-to-back induce an opposition to the crossing of electrons, and give rise to the higher resistance values at those contact points.[111] Owing to that, all grains would have an electron depletion region, the conductivity of a grain network would be limited by the presence of the potential barrier at the interconnection between grains, as shown in figure 4. The height of the potential barrier relies on the thickness of the depletion layer and grains connectivity.

According to Bochenkov *et al.*,[112] there are three different cases of conductance mechanisms that can be distinguished regarding the relationship between the space charge layer and grain size.

- Large grains with completely depleted contacts: large grain refers to grains which size (D) is larger than the thickness of the depletion layer (L) (Figure 6 (upper side)). This case appears when the grains are not sintered together, in such a situation there is not overlapping of the structures. The conductivity of the sensing film relies on the inner mobile charge carries and the electrical conductivity depends on the grain boundary control, which is not so sensitive to charges acquired from surface reactions.
- Large grains with partly depleted contacts: as D becomes smaller and comparable to 2L, necks become most resistant, and they start controlling the gas sensitivity (Figure 6 (middle side)). In this case, the contact does not play an important role in gas detection due to neck formation. The conduction

relies on the relative dimensions of the depletion layer and neck.[108] For a narrow neck, the depletion layer will generate an additional potential barrier in charge carriers. According to Korotcenkov *et al.*[14] narrow neck forms often constitute the most sensitive sites of sensing materials since all the electrons from these narrow necks can be potentially tied up with the chemisorbed oxygen, giving rise to entirely electron-depleted resistive regions. On the other hand, necks large enough will allow inter-grain conduction similar to a bulk material does.

- Small grains: when the grain size is less than twice the depletion layer thickness, the grain is fully involved in the space-charge layer (Figure 6 (bottom side)). The grains' resistance dominates the chain's whole resistance and the gas sensitivity is controlled by the grains themselves.

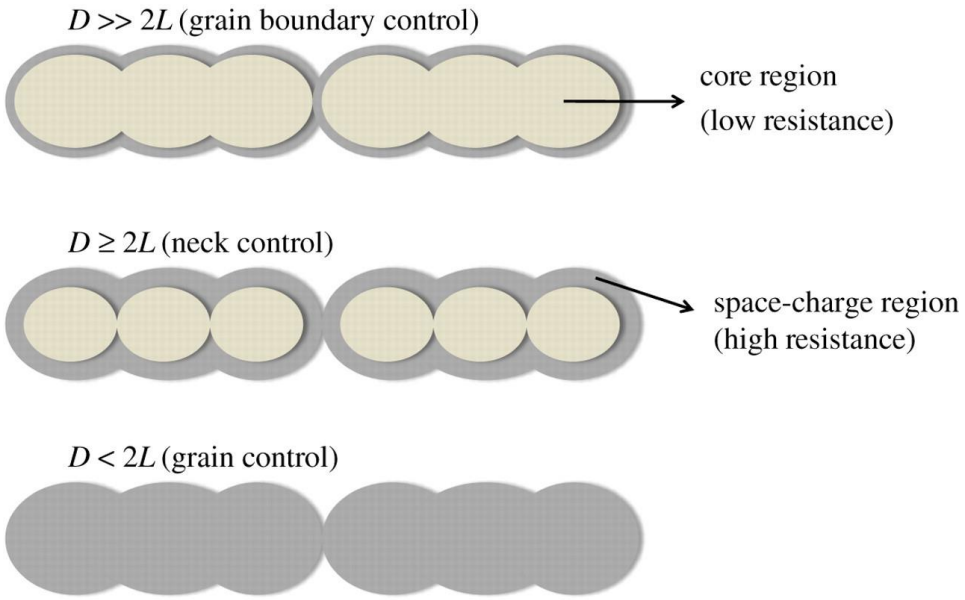


Figure 6 - Schematic model of grain size effect on electrical conductivity in porous film. The charge carries experiment different barriers according to the grain connections: grain boundary control $D \gg 2L$ (upper side), neck control $D \geq 2L$ (middle side) and grain control $D < 2L$ (bottom side).
Source: SHARMAN *et al.*[111]

Simultaneously, the conduction mechanism also depends on the type of gaseous species interacting at the semiconducting metal oxide surface since the density of the charge carrier varies. For an oxidizing atmosphere, the space-charge layer will become thicker (Figure 3.b)) until all active sites are occupied, whereas in the presence of reducing gases, the space-charge layer will become thinner (Figure 3.a)).

Large areas for absorption and the overlapping of grains are two critical parameters to consider for improving the gas sensing properties of semiconductor materials.

## 2.9 Sputtering deposition method

It has been reported that the gas sensor performance is strongly dependent on thin-film structure (grain size, shape, porosity, etc.); this, in turn, depends on both conditions of sintering and the preparation route used for thin-film formation. In particular, according to the synthesis method used, the same semiconductor metal oxide with similar morphologies presents different gas sensing properties.[14,113] Owing to the lack of this growth control, choosing among several deposition techniques the most indicated that permits the reproduction of the same sensing results from one film to the other is important. Sputtering, in this context, is an appealing technique to obtain such films considering that it allows high controllability of the process, time-saving, low deposition complexity, and film growth stability.[114]

The sputtering process consists of the physical removal of particles from a target surface (cathode) through the energy transfer of ionizing particles.[115] The outcoming atoms (from the target) are deposited on the substrate surface (anode), forming a film as shown in Figure 7. To reach the ejected atoms, an inert gas, such as argon (working gas), is injected into the vacuum chamber and employing a strong electric field between the cathode and anode causes the ionization of the inert gas, thereby allowing the acceleration of the ions toward the target material. Depending on how the ionizing potential is applied, the sputtering can be classified as direct current (DC) or radio-frequency sputtering (RF). Unlike DC sputtering, a constant voltage is used between cathode and anode, RF sputtering is applied to an oscillating voltage with a high-radio frequency. Furthermore, permanent magnets are placed in the immediate cathode vicinity to force electrons to rotate inside the plasma near the target and increase the collision probability and the ionization process.

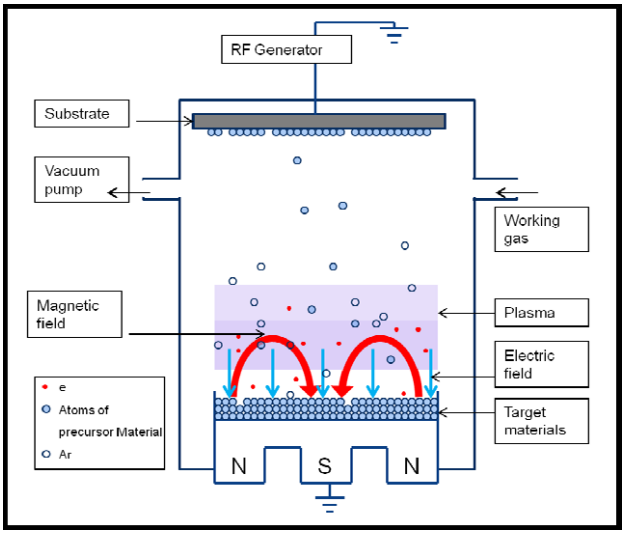


Figure 7 - Schematic representation of RF magnetron sputtering.
Source: BOSCO *et al.*[116]

# 3 OBJECTIVES

This project aims to synthesize ITO and rGO/ITO thin films by RF magnetron sputtering and verify how variations in deposition parameters affect sensing properties regarding ozone gas detection.

For this purpose, the next specific objectives were established:

- Synthesize ITO and rGO/ITO thin films by RF magnetron sputtering from an ITO ceramic target.
- Analyze the effect of heating, ex- and in- situ process as well as deposition atmosphere on microstructure.
- Analyze the film growth conditions on microstructure and crystallinity of ITO and rGO/ITO thin films.
- Study the microstructure influence on the gas sensing properties of ITO and rGO/ITO thin films.

# 4 MATERIALS AND METHODS

All experimental work is divided into three important sections (Figure 8): thin film deposition, structural and chemical characterization and, finally, the evaluation of the gas sensing properties. In the first part of the work, ITO thin films are deposited under two deposition types (Ex- and In- situ process), and their influence on the structure and morphology of ITO film is studied. To find the deposition types that enhance the sensing properties, the response of ITO sputtered films to ozone is investigated. Finally, the deposition type of the ITO sensor with a good response is undergone two further depositions: ITO film deposited (i) by changing sputtering atmosphere and (ii) on the rGO surface.

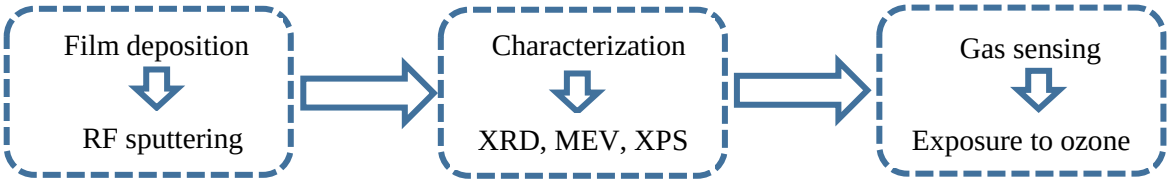


Figure 8 - Work plan scheme for the study of ITO films used as a gas sensor.
Source: By the author.

## 4.1 Experimental procedure

### 4.1.1 The cleaning process and substrate functionality

Three different substrates were used for deposition and characterization purposes: glass, silicon and interdigitated electrodes-containing silicon. The substrates were degreased in a dilute detergent solution, rinsed ultrasonically in deionized water, dried in a furnace in air, and finally, they were cleaned in a piranha solution bath. The glass, silicon and interdigitated electrode-containing silicon substrates were used during the preparation of ITO thin films and rGO/ITO composites. The glass and interdigitated electrode-containing silicon substrates were intended for XRD and gas sensing measurements, respectively, whereas silicon substrate was intended for XPS, MEV and AFM measurements.

### 4.1.2 ITO deposition

ITO thin films were deposited on various substrates by RF (13.5 MHz) magnetron sputtering technique from a ceramic ITO target containing 90 wt% $In_2O_3$ and 10 wt% $SnO_2$. Prior to deposition, the chamber was evacuated to a background pressure of $4.5x10^{-6}$ mbar, and then by injecting Ar or Ar+$O_2$ the working pressure was fixed at $2.5x10^{-2}$ mbar. The Ar and $O_2$ flow rates were adjusted by two independent mass flow controllers. The RF power and target-to-substrate distance were 60 W and 6.5 cm, respectively. These parameters were fixed for all depositions (Table 2). In the first part, the deposition process was carried out in pure Ar atmosphere and the substrate temperature was changed (Figure 9.a)). The ITO films grown at room temperature were subsequently annealed at 200, 300, 400 and 500 °C for 1 h in air. Table 3 indicates the type of annealing previously mentioned. Then the films prepared under the optimized deposition parameters were subjected to two further depositions as shown in Figure 9.b), as follows: ITO films were deposited (i) under a pure Ar and an Ar+$O_2$ atmosphere (6.6 % $O_2$ content), (ii) on the rGO surface combining the sputtering atmospheres mentioned before. And finally, ITO films and rGO/ITO were annealed at 300 °C under air for 1 h. The deposition conditions for the second part are summarized in table 4. The heating rate used in the oxidation processes was 2.5 °C/min. Before each deposition, a 5-7 min pre-sputtering process was employed to clean the target surface. In our experimental conditions, the different thicknesses were controlled by the following deposition rates: 23.3 nm/min for Ar atmosphere and 7.9 nm/min for Ar+$O_2$ atmosphere (6.6 % $O_2$ content).

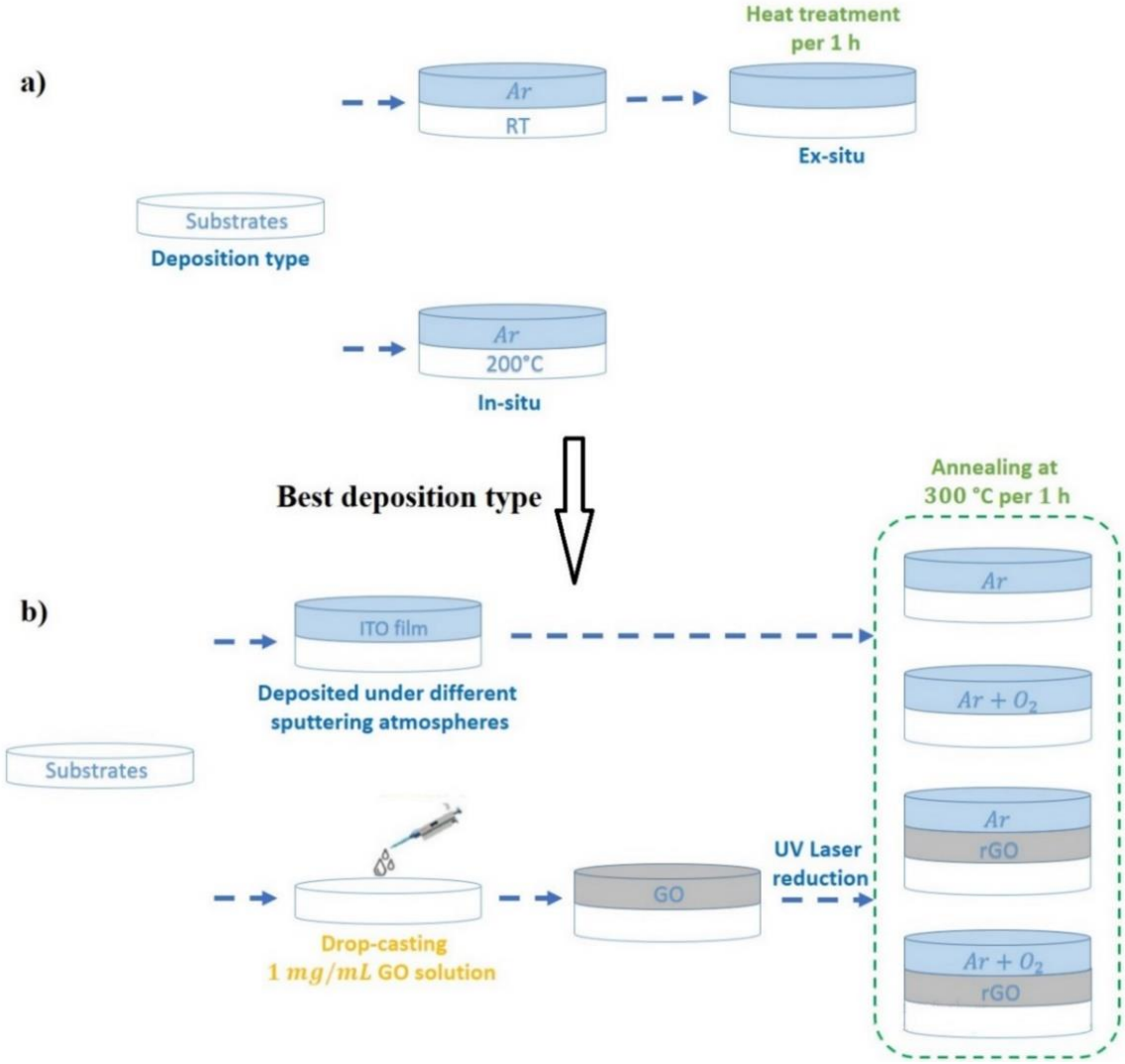


Figure 9 - Schematic representation showing the procedure conducted to obtain a) the ITO films under two deposition types and b) the rGO and rGO/ITO composites.
Source: By the author.

Table 2 - Deposition parameters used to obtain ITO tin films and rGO/ITO composites by RF magnetron sputtering

| Parameters | Values |
|---|---|
| Base pressure | $4.5x10^{-6}$ (mbar) |
| Working pressure | $2.5x10^{-2}$ (mbar) |
| Sputtering gas | Pure Ar or Ar+$O_2$ (6.6 % $O_2$) |
| Power | 60 W |
| Substrate-target distance | 6.5 cm |

Source: By the author

Table 3 - ITO samples and type of annealing conducted during the first part of the deposition process

| Nomenclature | Sputtering atmosphere | Substrate temperature (°C) | Heat treatment (°C) | Type of annealing |
|---|---|---|---|---|
| ITO0 | Ar | RT | - | - |
| ITO1 | Ar | RT | 200 | ex-situ |
| ITO2 | Ar | RT | 300 | ex-situ |
| ITO3 | Ar | RT | 400 | ex-situ |
| ITO4 | Ar | RT | 500 | ex-situ |
| ITO5 | Ar | 200 | - | in-situ |

Source: By the author

Table 4 - ITO films deposited under two different atmospheres or on the rGO surface for the second part of the deposition process.

| Nomenclature | Sputtering atmosphere | Substrate temperature (°C) | Heat treatment (°C) | Type of annealing |
|---|---|---|---|---|
| S-1 | Ar | RT | 300 | ex-situ |
| S-2 | Ar+$O_2$ | RT | 300 | ex-situ |
| S-3[ii] | Ar | RT | 300 | ex-situ |
| S-4[iii] | Ar+$O_2$ | RT | 300 | ex-situ |
| S-5[iv] | Ar+$O_2$ | RT | 300 | ex-situ |

Source: By the author

### 4.1.3 Preparation of rGO compound

The graphene oxide (GO) was prepared by the modified Hummer's method[117] and the rGO was then obtained using UV laser radiation.[118] An aqueous solution of graphene oxide was diluted to 1 mg/ml. Then, this solution was drop-casted on a heated substrate and, four cycles of $25\,\mu L$ each were used in the drop-casting procedure (Figure 9.b)). The laser reduction process was carried out in ambient conditions using a Spectron SL400 Nd:YAG

[ii] The sample S-3 is short for rGO/Ar
[iii] The sample S-4 is short for rGO/Ar+$O_2$
[iv] The sample S-5 is short for rGO/Ar+$O_2$

laser system in which the pulse duration and wavelength were set to 6 ns and 266 nm, respectively. The substrates with the deposited GO films were placed on a XY table that scanned the film at a scanning rate of 1 mm/s. Figure 10 shows an illustration of the process performed for reducing GO. After the reduction process, the rGO films were introduced into the RF magnetron sputtering chamber under the deposition conditions established in section 4.1.1.

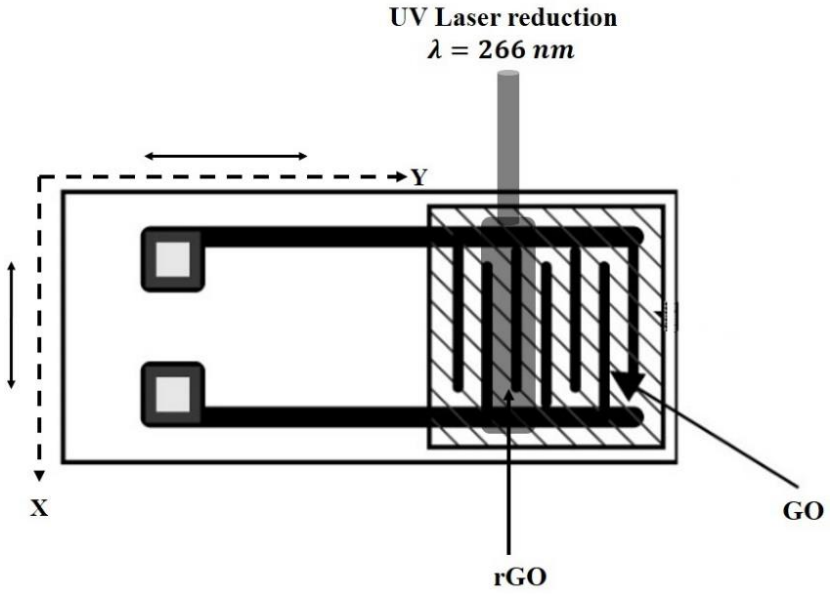


Figure 10 - Schematic presentation showing the procedure to obtain rGO film.
Source: Adapted from ARSHAK *et al.*[119]

## 4.2 Samples characterization

The structural properties of ITO films and rGO/ITO composites were conducted by X-ray diffraction. The X-ray diffraction date were collected in a Rigaku Ultima IV diffractometer equipped with a Cu target, Cu-$K_\alpha$ radiation ($\lambda = 1.5418\ \dot{A}$). The recording of the diffraction patterns was made with a 0.02º step from $2\theta = 20$ to 70°. The XDR patterns were compared with the pattern reported in crystallographic database ICSD (Inorganic Crystal Structure Database). The surface roughness and morphology of the prepared films were characterized using atomic force microscopy (AFM, Bruker Dimension ICON, tapping mode), scanning electron microscopy (SEM, JEOL JSM-7500F). The chemical composition and oxidation state of the elements present on the surface of the ITO films and rGO/ITO composites were by X-ray photoelectron spectroscopy (Scinta-Omicron ESCA+, Al $K_\alpha$ source (1486.7 eV)). The XPS spectra were adjusted using Shirley's background subtraction

method, and the peaks were adjusted by mixed Gaussian-Lorentzian curves. The obtained spectra were corrected, assuming 284.8 eV for adventitious carbon. The data analysis was accomplished by CasaXPS software.

### 4.3 Gas sensing measurements

To build the gas sensor, the ITO thin films and rGO/ITO thin film composites were deposited on Pt interdigitated electrodes printed in silica substrates ($SiO_2$/Si) containing 100 nm thick Pt interdigitated electrodes (Figure 11 (a)). The interdigitated electrodes were fabricated by sputtering and photolithography techniques in the Microfabrication Laboratory (LMF) at the Brazilian Synchroton Light Laboratory (LNLS). Figure 11 (b) shows the experimental setup used to measure the gas sensing properties of ITO thin films and rGO/ITO composites under pollutant gas. The sensors are placed on a heating plate inside a sealed chamber equipped with a gas inlet and outlet. The sensing properties were determined by the continuous monitoring of the electrical resistance changes of the films during exposures of controlled ozone concentrations. Using two needles on electrode extremes, the electrical resistance is monitored continuously by measuring the electrical current with a Keithley 6514 electrometer when an excitation voltage of 1 V is applied between electrodes. The Mass Flow Controllers, electrometer, voltage source, and temperature controller were connected to a computer dedicated to experimental controlling and data acquisition.

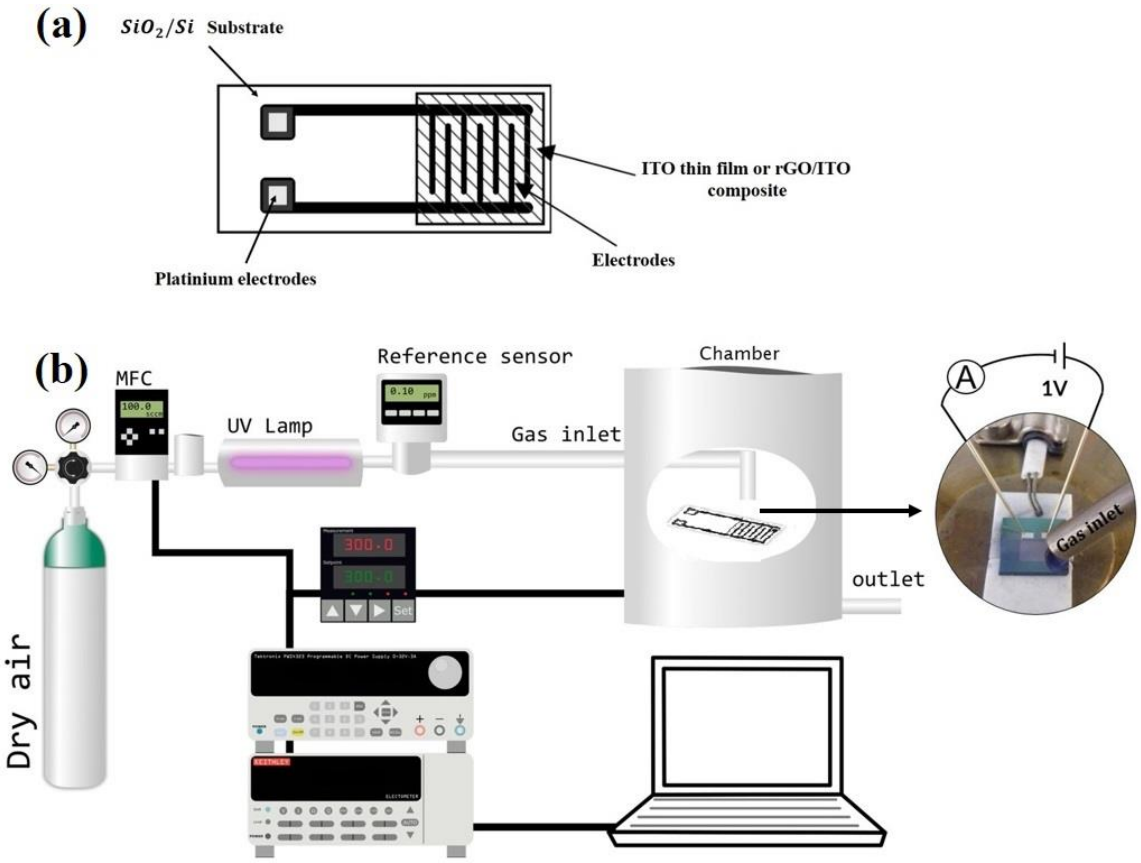


Figure 11 - (a) Scheme of printed interdigitated electrodes and (b) gas sensing properties measurement setup. Source: (a) Adapted from ARSHAK *et al*.; [119] (b) DE LIMA *et al*.[120]

The ozone-controlled exposures are carried out by exposing the dry air flow under UV radiation lamp (UVP, model P / N 90-0004-01), and the ozone concentration is determined by a commercial AT1 (model F12) commercial electrochemical based gas detector. The different ozone concentrations were determined through a rule, in which each position means a well-known ozone concentration. While the temperature is controlled, a mixture of dry air and ozone is injected above the sample, where the total flow used is 100 sccm All the gas sensing measurements were conducted under relative humidity at between 19 to 21 %.

The baseline is acquired when injecting dry air without ozone. The sensitivity (S) is defined as $S(\%) = \left(\frac{R_{O_3}}{R_a} - 1\right) * 100$, where $R_{O_3}$and $R_a$ are the electrical resistances measured in the presence of ozone and dry air, respectively. The response/recovery times are defined as the time taken by sensor to reaching 90 % of $\Delta R$ induced by pollutant concentrations during gas exposure and consecutive recovery under dry air.

# 5 RESULTS

## 5.1 Characterization of ITO thin films: Effects of ex- and in- situ processes on the structure and morphology in pure Ar atmosphere.

Figure 12 shows the X-ray diffraction (XRD) patterns of the as-deposited (ITO0 and ITO5) and annealed ITO films (ITO1-ITO4) deposited on glass substrates through RF-magnetron sputtering with thicknesses just above 1 $\mu m$. Figure 12) shows that the ITO5 film, which corresponds to the sample deposited at 200°C, displays a crystalline structure as well as a preferential orientation along the (400) plane, while when the substrate is not heated during deposition (ITO1 film) no diffraction peaks are observed, indicating an amorphous state of the deposited film.

To reach the crystallization for the RT deposited ITO film, the samples were submitted to an ex-situ treatment at different temperatures in oxygen atmosphere. As shown in Figure 12), ITO1 sample is semi-crystalline, whereas ITO2 has a completely accomplished crystallization. The ITO1, ITO2 and ITO3 films exhibit the preferred orientation along the (222) plane. It is also observed that ITO4 presents a slightly preferred orientation change from (222) to (400) peak. All the diffraction peaks of the crystalline ITO thin films can be indexed to the cubic bixbyite structure with JCPDS card No: 06-0416 and the space group of Ia3 (206). This result suggests that the $Sn^{+4}$ ions occupy the $In^{+3}$ ions sites in the $In_2O_3$ crystal structure, and therefore, there were no other peaks corresponding to impurity relating to Sn, SnO or $SnO_2$ phases. The preferred orientation along (400) appears when the film is sputtered in an oxygen-deficient atmosphere, indicating that these planes' oxygen vacancies are accommodated. On the other hand, owing to the annealing was conducted under an oxygen-rich atmosphere, stoichiometric $In_2O_3$ maintains and the crystal growth is preferentially with (222) plane. This plane does not accommodate oxygen vacancies very well, and so it is stabilized when there are fewer oxygen vacancies. These results are consistent with the previously reported data.[40,54,55,59] The orientation of the films is thought to be dependent on the mobility of atoms on the substrate.[62] If the atoms have a sufficient amount of energy, the ITO films will be orientated along the thermodynamically favorable plane or direction. When the substrate temperature is low, the mobility of atoms and particles deposited on the substrate is reduced, then the probabilities of interaction are also reduced, which results in an amorphous state. Whereas high substrate temperature increases the mobility of atoms, leading

to a crystalline structure of ITO films. The amorphous film has many defects and nonstoichiometry in composition. Post-deposition annealing can oxidize nonstoichiometry composition, and rearrange atoms to form stable polycrystalline films.[121]

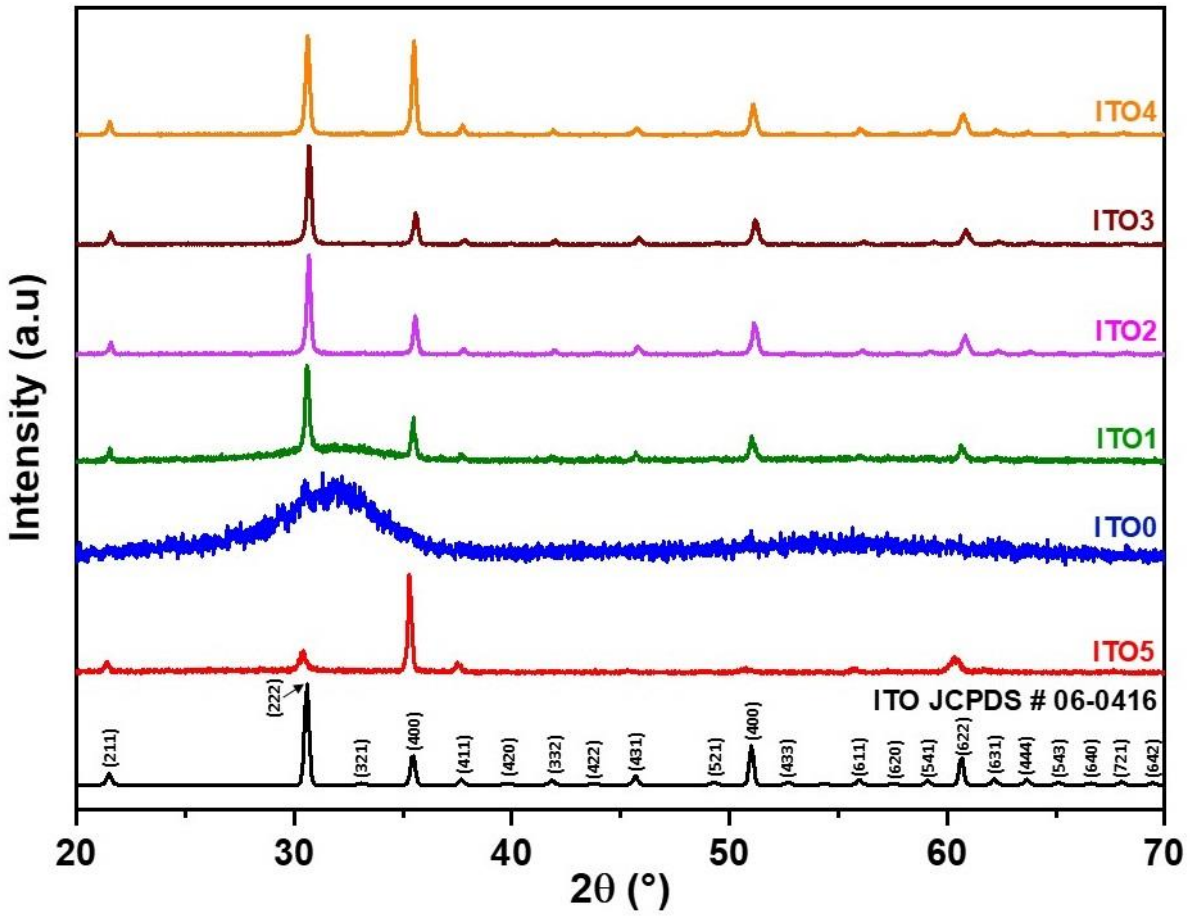


Figure 12 - XRD patterns of ITO thin films deposited under different deposition types and heat-treatment in pure Ar atmosphere. ITO5 (deposited at 200°C), ITO0 (as-deposited), ITO1 (heat-treatment at 200°C), ITO2 (heat-treatment at 300°C), ITO3 (heat-treatment at 400°C) and ITO4 (heat-treatment at 500°C).
Source: By the author

To study the effect of the ex- and in- situ heat-treatment processes on the morphology of ITO films, three samples were selected for that purpose. Figure 13 shows the SEM images of ITO2, ITO4 and ITO05 with thicknesses of about 100 nm deposited on silicon substrates. Figure 13 (a, b) show the surface morphology and the grain size distribution of ITO5. It can be noticed that this film consists of two type of grain sizes, where the smaller grain sizes of 13 nm are tight across the film, while the larger ones of 38 nm present triangular and more dispersed grains. Figure 13 (c, d) depict the surface morphology of ITO2 and ITO4, respectively. Both films exhibit grain size formation with very small grains compared to ITO5 without any significant change in morphology between them. It also shows that the grain size distribution both for ITO2 and ITO04 is seemingly uniform and nearly the same. Although it

is impossible to determine the grain sizes both for ITO2 and ITO4 because of their tiny sizes, one can expect their average grain size to be under 13 nm.

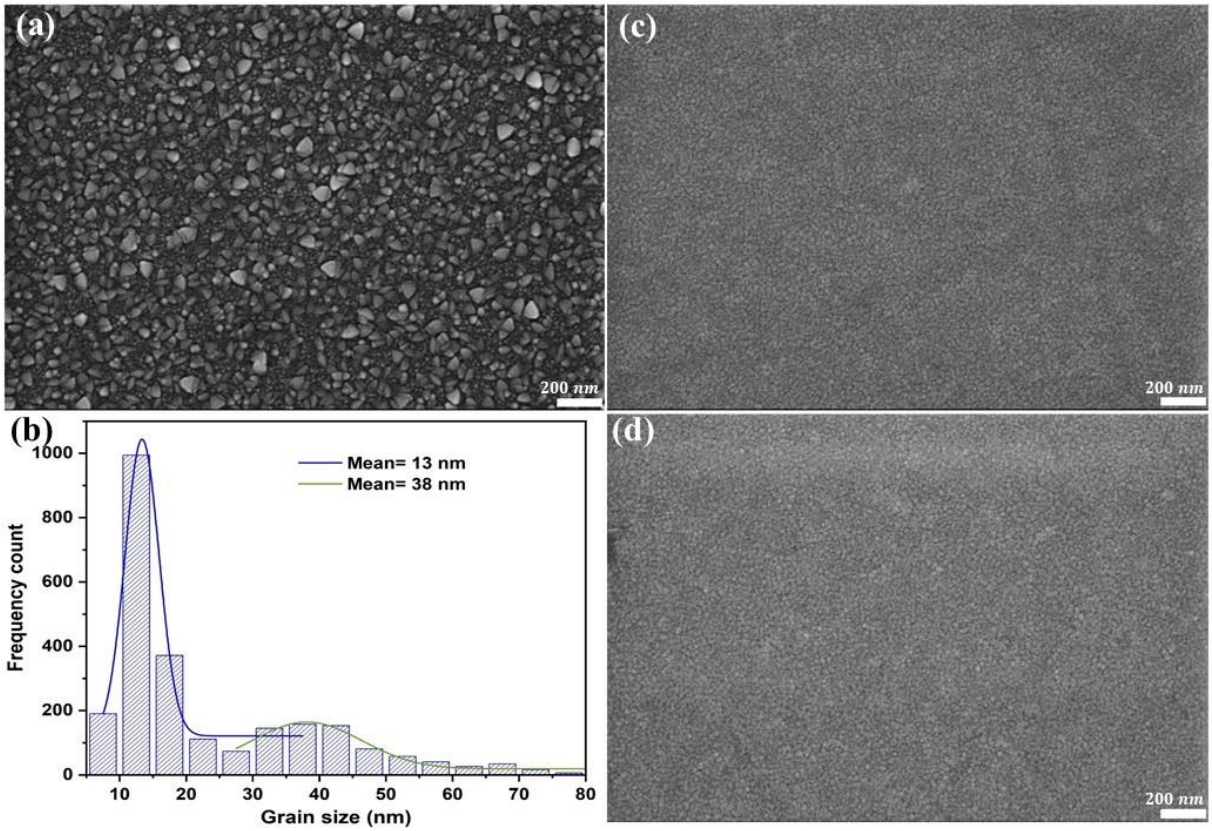


Figure 13 - SEM images of 100 nm thick ITO2, ITO4 and ITO5 on silicon substrate. (a) ITO5 (deposited at 200°C), (b) grain size distribution of ITO5, (c) ITO2 (heat-treatment at 300°C) and (d) ITO4 (heat-treatment at 500°C).
Source: By the author

In addition, the surface microstructure of ITO films obtained from ex-situ and in-situ processes was also analyzed by employing three-dimensional AFM images (scan area 1 $\mu m^2$) shown in Figure 14 on silicon substrates. It can be observed the effect of deposition type and the annealing on the surface morphology of ITO films. In the case of deposition type, that is, ex- and in-situ processes, Figure 14 (a) (ITO5) (sample deposited at 200 °C), as expected, shows grains that are closely packed and very dense with two nano-sized distributions, whereas Figure 14 (c) (ITO2) (sample heat-treated ex-situ at 300 °C) shows not only smaller grain sizes, but also much less dense grains, and hence a more porous film. In the case of annealing temperature, Figure 14 (d) (ITO4) (sample heat-treated ex-situ at 500 °C) exhibits just slightly larger grain sizes, a denser and thus less porous film than ITO2 is also observed. The mean surface roughness obtained from AFM images shows values of 0.73, 1.09 and 2.59 nm for ITO2, ITO4 and ITO5, respectively.

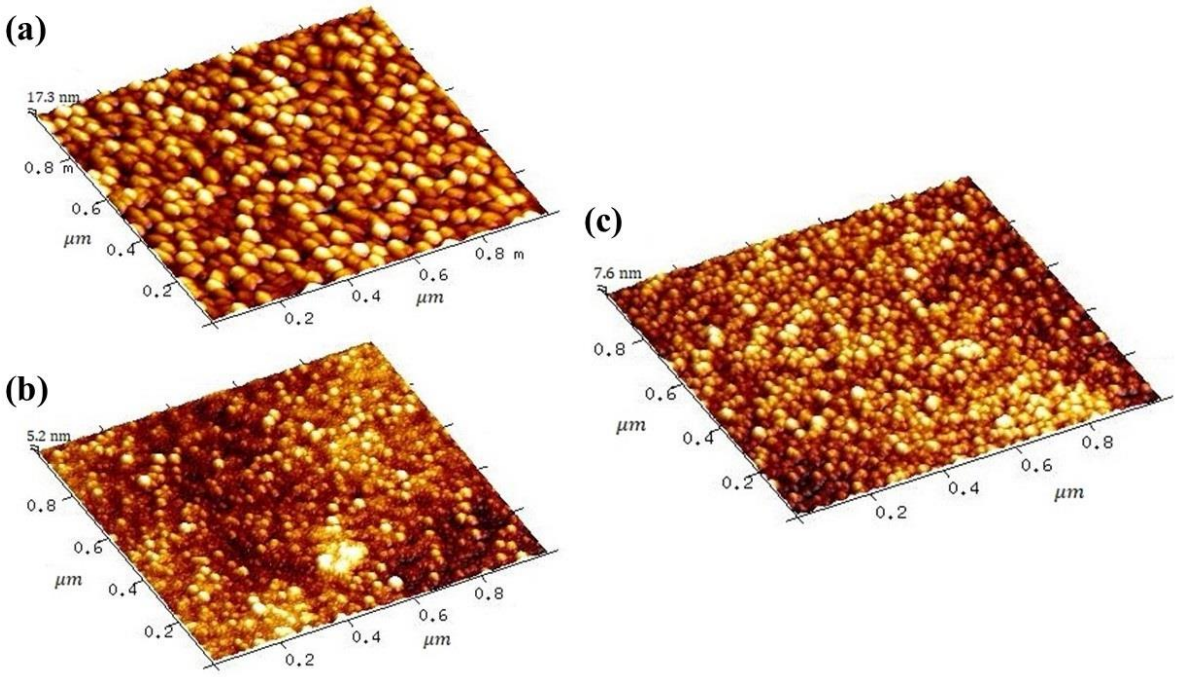


Figure 14 - AFM images of (a) ITO5 (deposited at 200°C), (b) ITO2 (heat-treatment at 300°C) and (c) ITO4 (heat-treatment at 500°C).
Source: By the author

## 5.2 Characterization of ITO thin films deposited under different atmospheres and on the rGO surface

Figure 15 shows the XRD diffraction patterns of the annealed ITO films (S-1, S-2) and annealed rGO/ITO films (S-3, S-4) on glass substrate. All the diffraction peaks of S-1, S-2, S-3 and S-4 have a single-phase diffraction pattern belonging to the ITO cubic structure (JCPDS # 06-0416). It can be noticed that the introduction of $O_2$ along with Ar during the preparation of ITO films presents a preferential orientation along the (440) plane, despite being heat-treated in an oxygen-rich atmosphere. However, the deposition of ITO under pure Ar or $Ar+O_2$ atmospheres on the rGO surface conserves the most typical orientation plane of $In_2O_3$ (the plane (222)) and any peak assigned to rGO is observed.

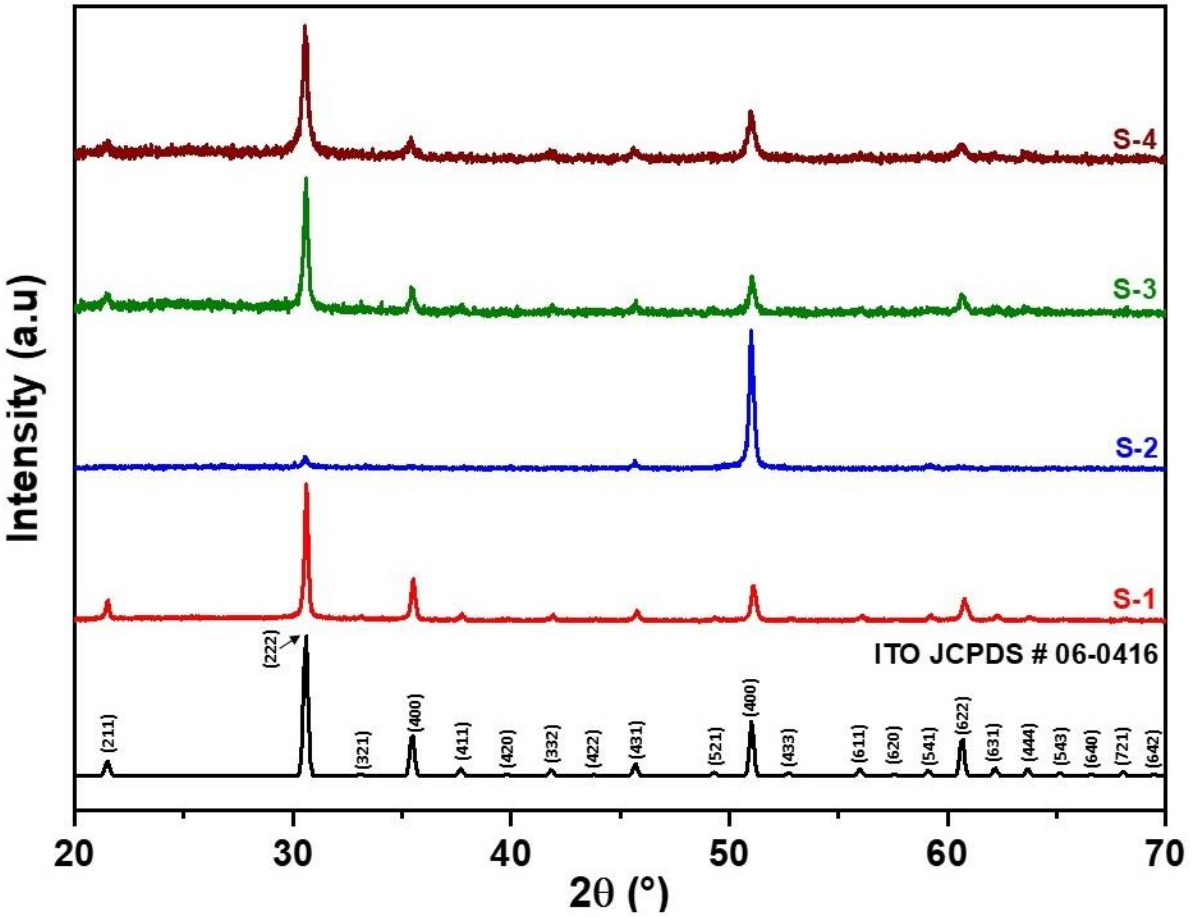


Figure 15 - XRD patterns of S-1, S-2, S-3 and S-4 on glass substrate. S-1 (deposited in pure Ar atmosphere), S-2 (deposited in $Ar+O_2$ atmosphere), S-3 (rGO/Ar) and S-4 ($rGO/Ar+O_2$).
Source: By the author

Figure 16 presents SEM micrographs of S-1, S-2, S-3 and S-4. Figure 16 (a, b) shows SEM images with equal magnification for S-1 and S-2. The sample S-2, grown with the $Ar/O_2$ mixture, results in slightly larger grain sizes compared to S-1 (deposited in pure Ar atmosphere). The average grain size values are expected to be between 11-13 nm and 11-15 nm for S-1 and S-2, respectively. Figures 16 (c, e) and (d, f) present two different magnifications for S-3 and S-4, respectively. One can note that the surface morphology of S-3 is very similar to that of the rGO surface structure (Figure A.1), whereas the surface morphology of S-2 is totally different from rGO and S-1 surfaces. It is clear that the use of $O_2$ is an important parameter to take into account during depositions of ITO thin films and rGO/ITO composites. On the one hand, it tends to form slightly larger grain sizes on ITO films and, on the other hand, apparently has an inhibitory effect on the rGO surface, and because of this, the sample S-3 turns to be much more porous than the sample S-4.

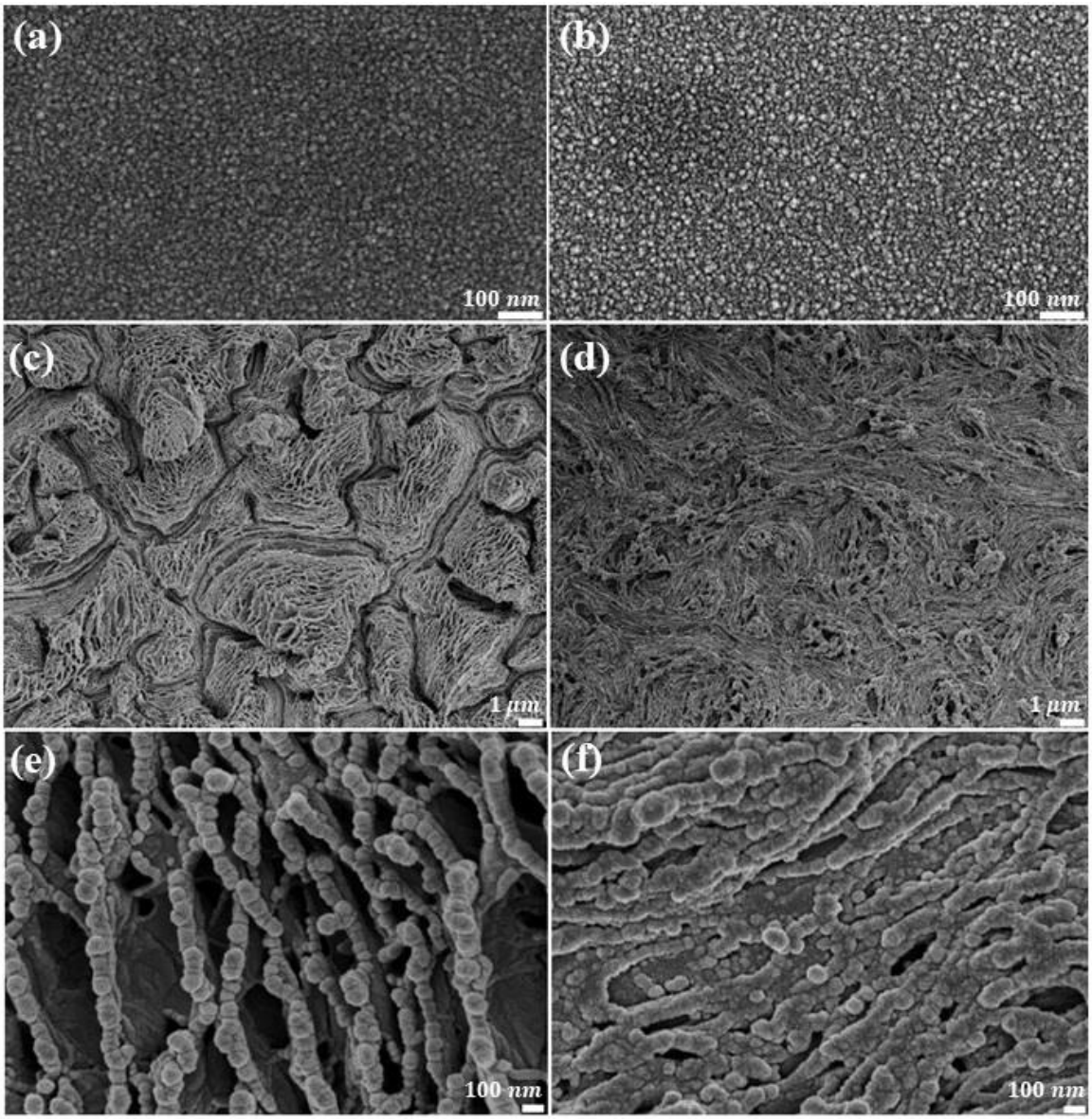


Figure 16 - SEM images of S-1, S-2, S-3 and S-4. (a) 100k magnification S-1, (b) 100k magnification S-2, (c) 5k magnification S-3, (d) 5k magnification S-4, (e) 50k magnification S-3 and (f) 50k magnification S-4. S-1 (deposited in pure Ar atmosphere), S-2 (deposited under Ar+$O_2$ atmosphere), S-3 (rGO/Ar) and S-4 (rGO/Ar+$O_2$).
Source: By the author

In order to confirm the element composition present at the surface and oxidized states of S-1 S-2, S-3, S-4 and S-5 samples, XPS characterization was conducted. Figure 17 shows the XPS survey spectra of S-1, S-2, S-3, S-4 and S-5 in the energy range of 0-1200 eV on silicon substrates. As can be seen, each survey scan confirmed the unique presence of peaks assigned to C, O, In and Sn. Carbon is presumably present as a surface contaminant originating from adsorbed $CO_2$ or hydrocarbons present in the air, as confirmed by analyses of high-resolution C 1s spectra of the five samples (see Figure A.2). These spectra show three different carbon types, namely, from low to high binding energies: C-C, C-O and O-C=O.

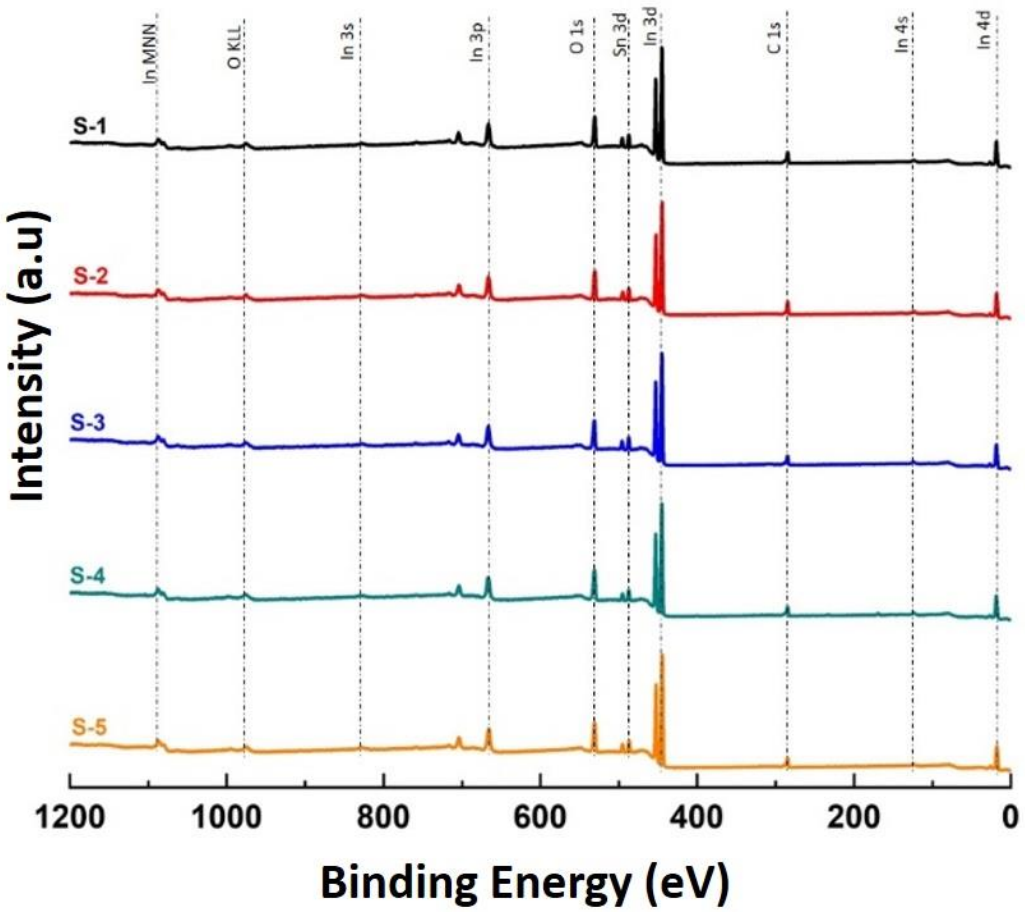


Figure 17 - XPS survey spectra of the samples S-1, S-2, S-3, S-4 and S-5. S-1 (deposited in pure Ar atmosphere), S-2 (deposited under $Ar+O_2$ atmosphere), S-3 (rGO/Ar), S-4 ($rGO/Ar+O_2$) and S-5 ($rGO/Ar+O_2$).
Source: By the author.

Figure 18 (a, b) exhibits the XPS spectra of In3d and Sn3d for S-1, S-2, S-3, S-4 and S-5. As shown in Figure 18 (a), there are two peaks for each sample, corresponding to the spin-orbit splitting of the In $3d_{3/2}$ and In $3d5_{/2}$ states. These correspond to the $In^{+3}$ bonding state, specifically $In_2O_3$.[17] Similarly, in Figure 18 (b) it can also be seen two characteristic peaks related to spin-orbit splitting of the Sn $3d_{3/2}$ and Sn $3d_{5/2}$ states, showing that Sn is present in the form of $Sn^{+4}$ originating from $SnO_2$.[17] This is consistent with the XRD results, where no other phases of $SnO_2$ were found.

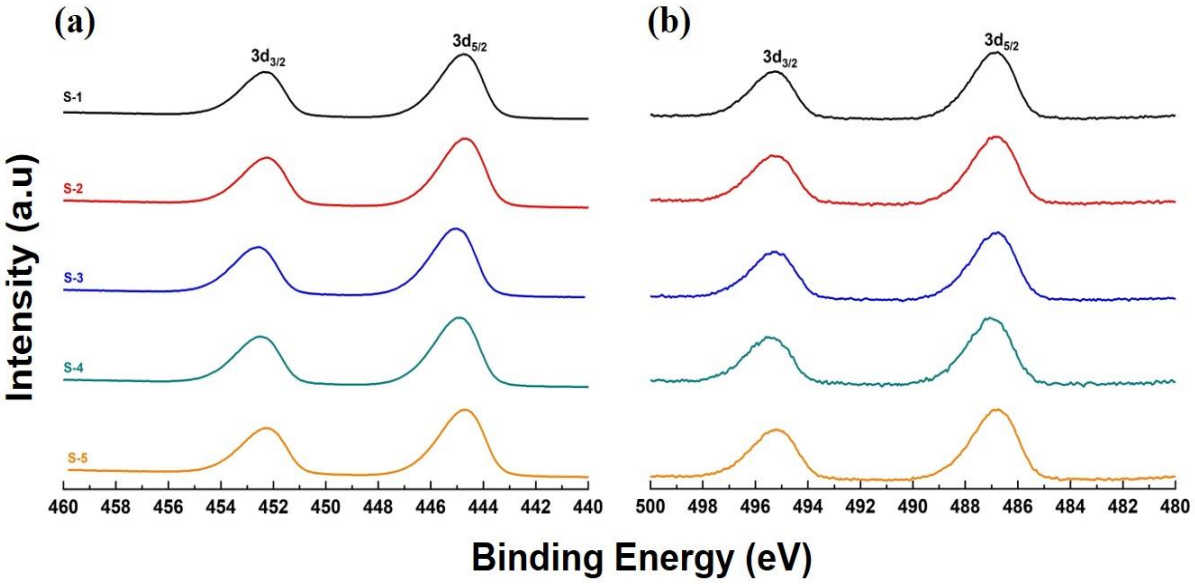


Figure 18 - XPS spectra of (a) In3d and (b) Sn3d of S-1, S-2, S-3, S-4 and S-5. S-1 (deposited in pure Ar atmosphere), S-2 (deposited under Ar+$O_2$ atmosphere), S-3 (rGO/Ar), S-4 (rGO/Ar+$O_2$) and S-5 (rGO/Ar+$O_2$).
Source: By the author.

Peak fits of high-resolution O 1s spectra for ITO films and rGO/ITO composites are shown in figure 19. The O 1s peak both for ITO films and rGO/ITO composites has been fitted with four components as follows: the lower binding energy (peak $O_I$) corresponds to the lattice oxygen of crystalline $In_2O_3$ in which In ions are fully bonded with neighboring $O^{2-}$ ions. The peak $O_{II}$ is associated to oxygen that is adjacent to oxygen-deficient sites. The third peak $O_{III}$ is attributed to absorbed OH groups or adsorbed oxygen species. And finally, the peak $O_{IV}$ is related to adventitious contaminants, specifically C-O and C=O.[122–124]

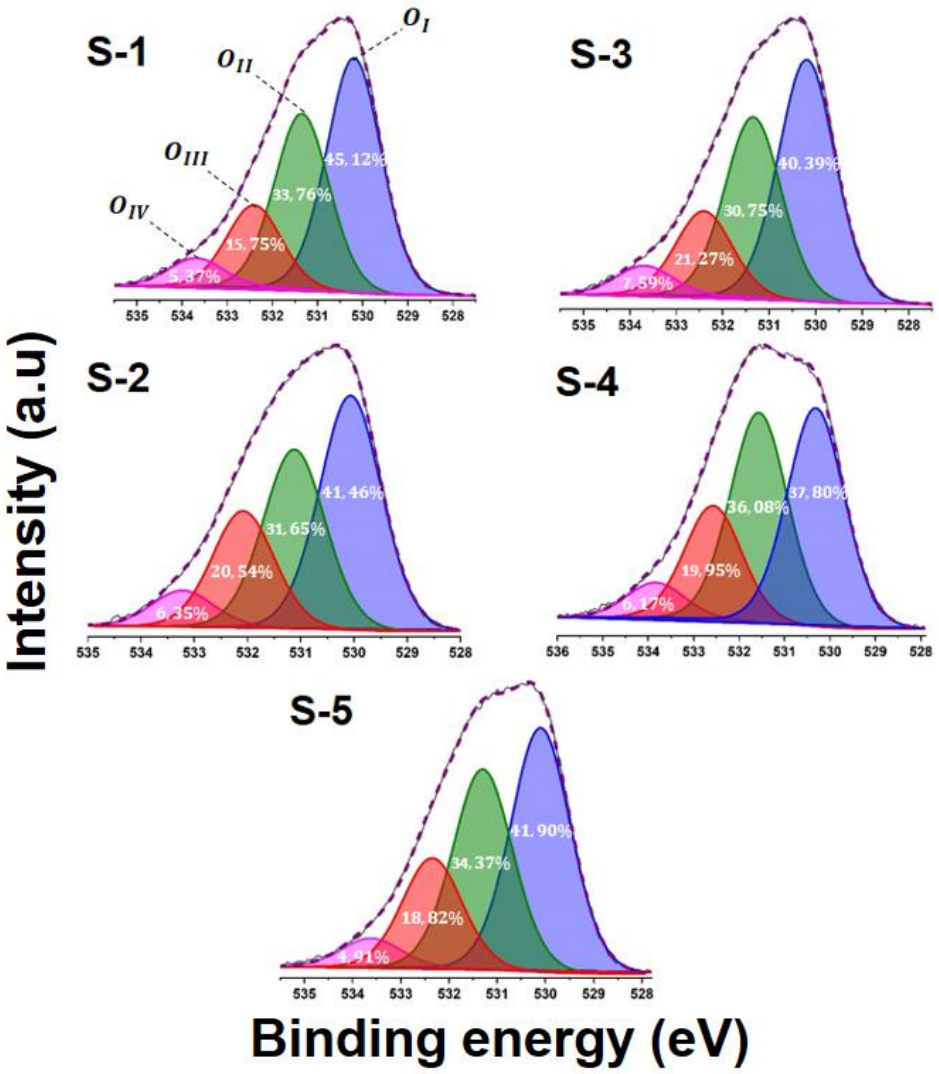


Figure 19 - High-resolution O 1s XPS spectra of S-1, S-2, S-3, S-4 and S-5. S-1 (deposited in pure Ar atmosphere), S-2 (deposited under Ar+$O_2$ atmosphere), S-3 (rGO/Ar), S-4 (rGO/Ar+$O_2$) and S-5 (rGO/Ar+$O_2$).
Source: By the author

## 5.3 Gas sensing properties towards $O_3$ detection of the ex-situ and in-situ processes

To determine the deposition condition that has the enhanced response regarding $O_3$, the ITO2, ITO4 and ITO5 samples with thicknesses of about 100 nm were selected. Figure 20 (a, b, c) shows the dynamic response-recovery curves obtained by monitoring the sensor's resistance when exposed to three cycles of 2.7 ppm $O_3$ at 200 °C for ITO2, ITO4 and ITO5. As it can be seen, the sensor resistance increases with $O_3$ inflow, which is typical behavior of a n-type semiconductor in presence of an oxidizing gas. One can also observe that upon the $O_3$ exposure time of 10 min, the higher resistance change was observed for the ITO2 sample, followed by that of ITO5. It is also clear after consecutive $O_3$ exposures, the selected samples

do not settle back to the original baseline resistance and tend to present higher baseline resistances. The average sensitivity values of the selected samples are shown in Figure 20 (d). The sensitivity values are 8.37, 1.89, 5.16 % for ITO2, ITO4 and ITO5, respectively. It is well known that there are several factors affecting the sensitivity, some of them are the grain size, surface roughness and porosity. Small grain sizes, high roughness values and porous films enhance sensor response. Although the samples ITO4 and ITO5 present the highest values in roughness (by AFM images), this is not the main parameter to explain the sensor responses shown in Figure 20 (d). It seems to be that porosity and grain size play the most important role in the senor response of these samples. Despite not having a great difference in morphology between ITO2 and ITO4, ITO2 exhibits a much porous surface that, along with its lightly smaller grain size, helps enhance the sensing response to ozone. This could explain the higher sensitivity of ITO2 as compared with ITO4 and ITO5. This means the best deposition condition in response to $O_3$ is the sample heat-treated ex-situ at 300 °C (sample under our experimental conditions ITO2).

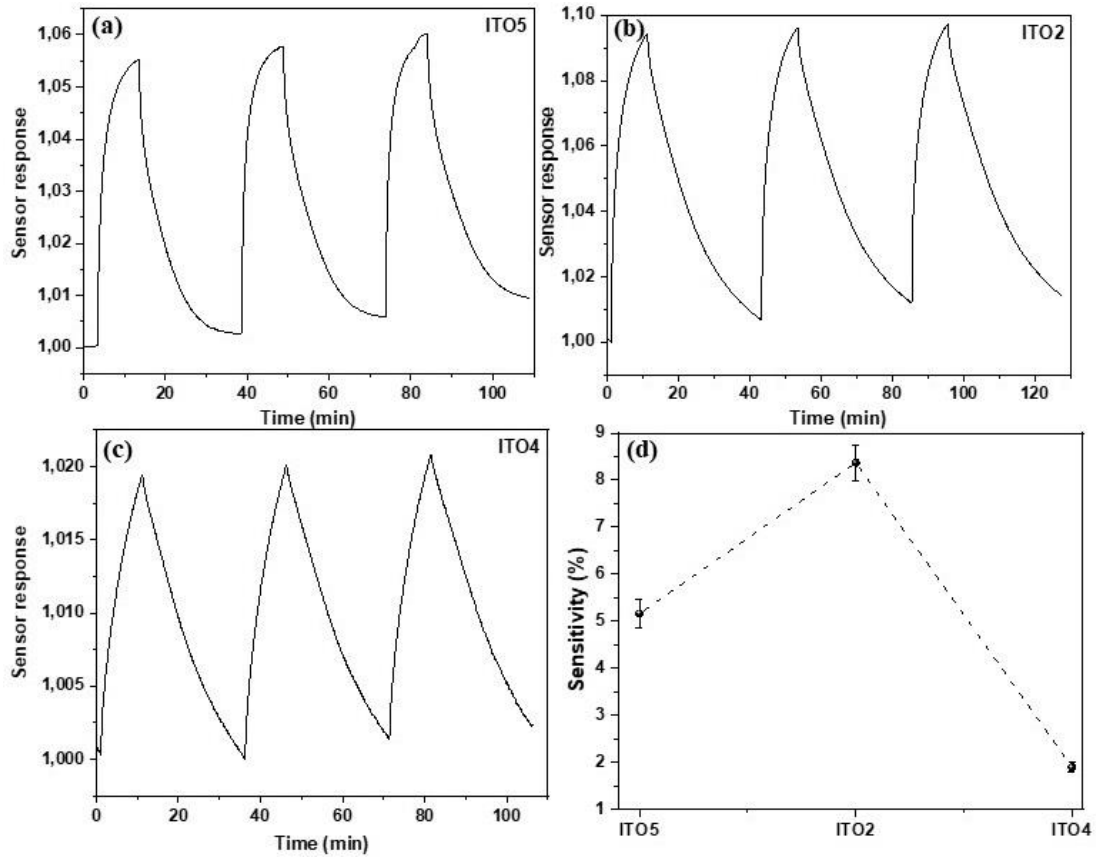


Figure 20 - (a-c) Dynamic response-recovery curves of the selected samples ITO2, ITO4 and ITO5 with thicknesses around 100 nm at the $O_3$ gas concentration of 2.7 ppm under 200 °C, and (d) their corresponding sensitivity. ITO5 (deposited at 200°C), ITO2 (heat-treatment at 300°C) and ITO4 (heat-treatment at 500°C).

Source: By the author

To determine the optimal operating temperature as to ITO2, its sensing performance towards 2.7 ppm $O_3$ at temperatures varying from 150 to 300 °C was investigated. According to Figure 21, the resistance variation increases and response/recovery times are shorter as the operating temperature increases. The highest sensitivity and lowest response/recovery time were at the working temperature of 300 °C with 13.53%, 4.11 min/8.50 min respectively. Two major processes are held on the surface of sensing materials during the gas sensing detection: the absorption of gas molecules and the transfer of electrons between gas molecules and sensing materials. These two processes are both subject to the working temperature of gas sensors. At low temperatures, the thermal energy is not enough to overcome the activation energy barrier. The likelihood of capturing gaseous species on the surface is low, which results in insufficient sensing reaction. On the contrary, at high temperatures the activation energy barrier decreases, but leads to free desorption of chemisorbed gas molecules from the surface of sensing materials before the reaction occurs, which also reduces the sensitivity of gas sensors.[17] Hence, in our selected temperate range, 300 °C[v] was selected as the optimal operating temperature in the subsequent test of gas sensitivity.

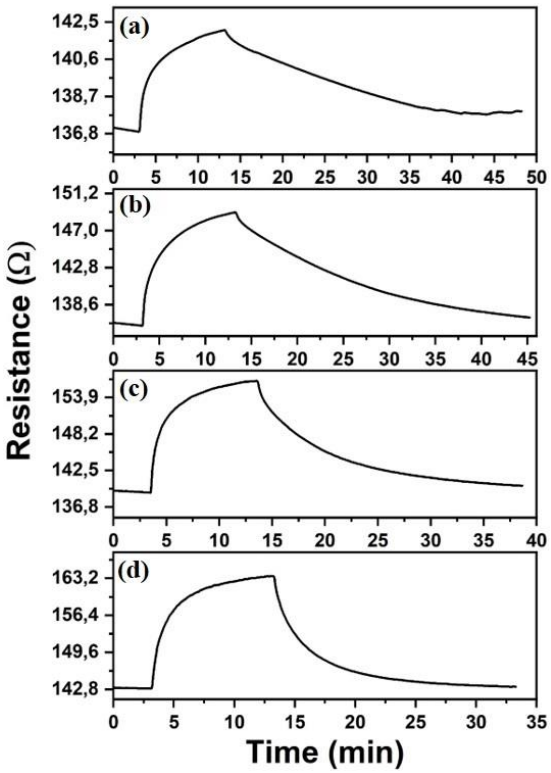


Figure 21 - Dynamic response-recovery curves of ITO2 upon exposure to 2.7 ppm $O_3$ at the operating temperatures of (a) 150 °C, (b) 200 °C, (c) 250 °C, (d) 300 °C. ITO2 (heat-treatment at 300°C).
Source: By the author

[v] Temperatures above 300 °C were not realized because the maximum temperature permitted in the heating system is precisely 300 °C.

Besides the study of the sensor behavior as a function of operating temperature, we also realized the sensing performance in terms of thickness for ITO2 under 300 °C and exposed to constant $O_3$ concentration, the results are shown in Figure 22. The response-recovery curves were measured under three cycles of 2.7 ppm $O_3$ for 10 minutes of exposure (Figure 22 (a)). It is possible to observe that the highest sensitivity was observed for the sample with 100 nm, as point out in Figure 22 (b). Interestingly, the sensitivity decreases either for smaller or greater thicknesses than 100 nm. It is important to mention the relationship between film thickness, grain size and porosity. As the thickness decreases, the grain size decreases, increasing the surface area, which implies enhanced sensitivity and shorter response/recovery times (Figure 22 (c)). Nonetheless, the thinner the film, the less porous the microstructure will be, decreasing the sensor's sensitivity. These two competing effects can explain the dome-like behavior (Figure 22 (b)) for the different thicknesses of ITO2, the maximum sensitivity of which is in the vicinity of 100 nm. In summary, under the ex-situ process conducted at 300 °C (sample ITO2) we obtained that the best operating temperature and thickness are 300 °C and 100 nm, respectively, towards ozone detection.

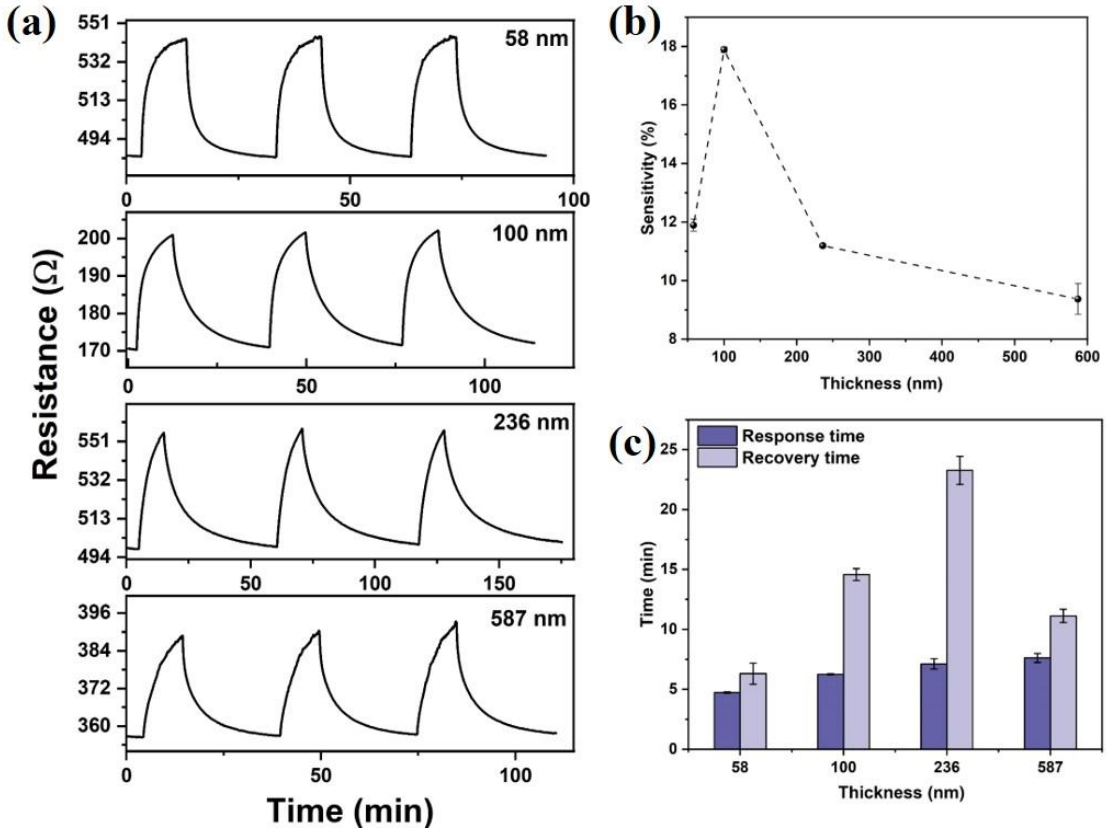


Figure 22 - (a) Dynamic response-recovery curves, (b) sensitivities, and (c) response/recovery times of ITO2 with thicknesses of 58, 100, 236 and 587 nm at the working temperature of 300°C and the ozone concentration of 2.7 ppm.

Source: By the author

Once the best deposition condition towards $O_3$ detection showed to be ex-situ process (sample ITO2), we realized the respective depositions of the second part of the work established in section 4.1.1. From now on, the sample ITO2 is named S-1. Table 5 displays the information of the other samples that will be used in the following step[vi]. It is worth noting that the thickness values shown in Table 5 are related to deposited ITO amount on rGO surface and not as rGO/ITO as a whole.

Table 5 - Names of the samples that are used in the second part of the work. S-1 (deposited in pure Ar atmosphere), S-2 (deposited under Ar+O2 atmosphere), S-3 (rGO/Ar), S-4 (rGO/Ar+O2) and S-5 (rGO/Ar+O2).

| Nomenclature | Thickness (nm) ~ |
|---|---|
| S-1 | 100 |
| S-2 | 100 |
| S-3 | 100 |
| S-4 | 100 |
| S-5 | 25 |

Source: By the author

## 5.4 Gas sensing properties to $O_3$ detection of ITO films under different sputtering atmospheres and on the rGO surface

Figure 23 (a) exhibits the response-recovery curves of S-1 and S-2 maintained at 300 °C upon exposing a constant $O_3$ concentration of 2.7 ppm. Both the S-1 and S-2 sensors show good reliability and reproducibility upon consecutive $O_3$ exposures. One can also observe that, after 10 min of $O_3$ exposure, the sensor signals both for S-1 and S-2 are very different. While S-1 presents a sharp form, S-2 looks like a rectangular one. Even though S-2 has a small resistance change as compared with S-1, it shows rapid response and recovery times, and a plateau for the resistance is reached. In fact, the average sensitivity values, response and recovery times are 17.88 %, 6.24 min/14.56 min for S-1 and 7.11 %, 2.24 min/1,28 min for S-2, respectively. Figure 23 (b-c) show the dynamic response-recovery curves and sensitivity values at 300 °C of S-1, S-2, S-3, S-4 and S-5 upon exposing varying $O_3$ concentration. Figure 23 (b) displays that the five sensors show a decreasing ladder-type shape with the

[vi] To observe the complete information of these samples, go to table 4 in section 4.1.1.

concentrations of $O_3$ decreasing from 650 to 140 ppb. It can be seen that the sensor S-1 and S-3 have higher resistance changes in response to $O_3$ compared to S-2, S-4 and S-5. The sensors S-1 and S-3 maintain their sharp-pointed shapes for all $O_3$ concentrations. In the same way, the sensors S-2, S-4 and S-5 maintain their rectangular form for the all $O_3$ concentrations. The sensitivity values of S-1, S-2, S-3, S-4 and S-5 for each $O_3$ concentration are shown in Figure 23 (c). As mentioned before, the sensors S-1 and S-3 present enhanced sensitivity to $O_3$, but still, no significant difference in sensitivity between them is observed for all $O_3$ concentrations. On the flip side, the sensors S-4 and S-5 exhibit higher response regarding S-2 for the whole $O_3$ concentrations, even though their sensitivities are much lower than that the S-1 and S-3.

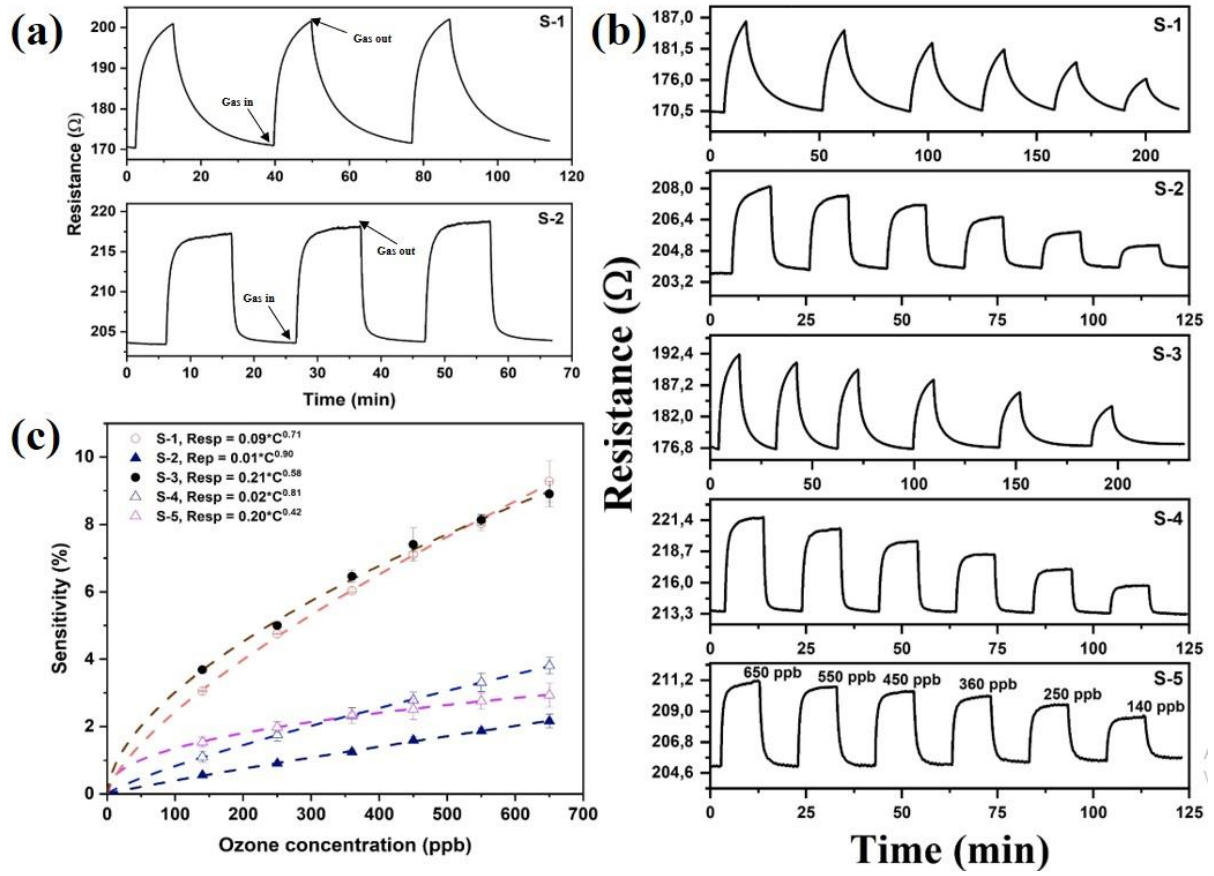


Figure 23 - (a) Dynamic response-recovery curves of S-1 and S-2 towards 2.7 ppm $O_3$ at 300 °C, (b, c) dynamic response-recovery curves and responses at 300 °C of S-1, S-2, S-3, S-4, S-5 to varying $O_3$ concentration. S-1 (deposited under pure Ar atmosphere), S-2 (deposited under Ar+$O_2$ atmosphere), S-3 (rGO/Ar), S-4 (rGO/Ar+$O_2$) and S-5 (rGO/Ar+$O_2$).

Source: By the author.

The response and recovery times represent the detection efficiency of gas sensors. Usually, strong gas adsorption on the material surface is very useful to improve the gas sensing properties. Nevertheless, the strongly adsorbed gas molecules are often difficult to

desorb from the sensing materials, which leads to slow recovery time. The response and recovery times of the sensors based on S-1, S-2, S-3, S-4 and S-5 upon exposure to different $O_3$ concentrations at 300 °C are exhibited in Figure 24. It is clear that the response and recovery times of S-2, S-4 and S-5 are much shorter than that of S-1 and S-3. Moreover, unlike S-1 and S-3, in which the recovery times are much larger than their response times, the recovery times of S-2 and S-4 are shorter than their response times for any $O_3$ concentration.

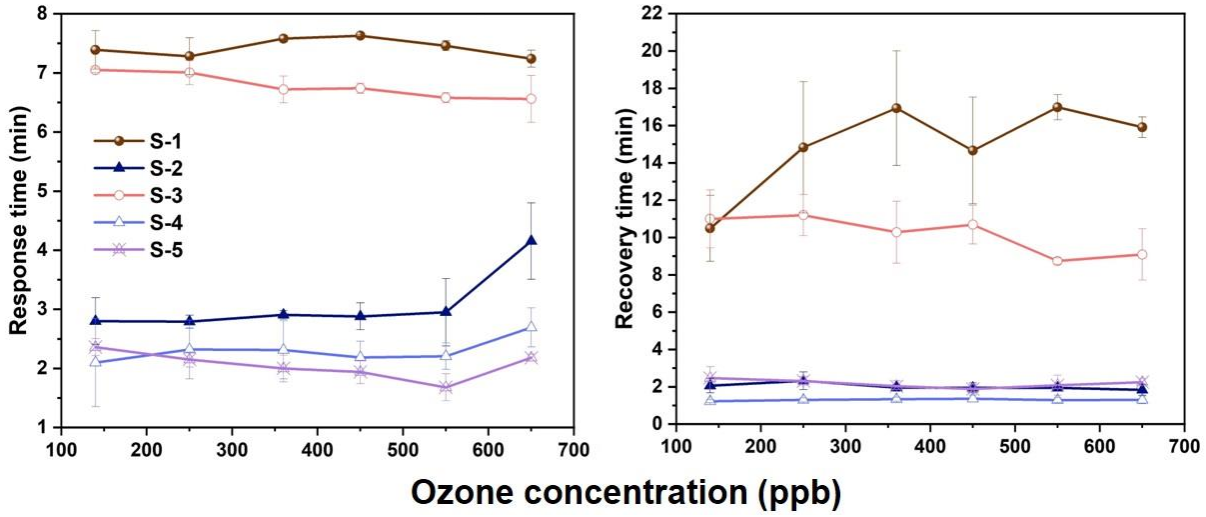


Figure 24 - Response and recovery time of S-1, S-2, S-3, S-4, and S-5 exposed to varying $O_3$ concentration at 300 °C. S-1 (deposited under pure Ar atmosphere), S-2 (deposited under Ar+$O_2$ atmosphere), S-3 (rGO/Ar), S-4 (rGO/Ar+$O_2$) and S-5 (rGO/Ar+$O_2$).
Source: By the author

It is widely known that one of the main reasons to use rGO with other materials further improving the gas sensing response is also to obtain that enhancement of performance at low operating temperatures. In that case, we compared the responses of the selected samples, namely S-3, S-4 and S-5, with the sample S-1. As a first comparison, the samples S-1 and S-3 were exposed to 2.7 ppm $O_3$ at 300°C and 250°C of operating temperature, respectively, as is shown in Figure A.3. As can be seen, by lowering the operating temperature for S-3, its sensor response is lower than that the S-1 response at 300°C, and even that response value is very close to that of S-1 at 250°C (Figure 21 (c)) at the same $O_3$ concentration, indicating that there is no enhancement on gas sensor performance. By contrast, the S-4 and S-5 samples exhibited a different sensor behavior by lowering operating temperature. For this case, these samples were exposed to 650 ppb $O_3$ at working temperatures of 300, 250, 200 and 150°C, as shown in Figure 25 (a, b). Both S-4 and S-5 tend to present higher sensor response with the decrease of the operating temperature to 200°C, then the response values fall down for S-4, and the signal was very weak for S-5, by further decreasing the operating temperature. It is clear that the S-5 sensor response is slightly higher with decreasing working temperature.

However, this is not the case for the sample S-4, the response of which is much higher. The sensing response of S-4 increases about three times at 200°C compared with itself at 300°C to 650 ppb $O_3$. Additionally, its sensing response is 1.31 times higher at 200°C than that of the S-1 at 300°C at the ozone amount of 650 ppb $O_3$, indicating that, among the rGO/ITO composites, the S-4 sensor displays a better response to $O_3$ at low working temperature.

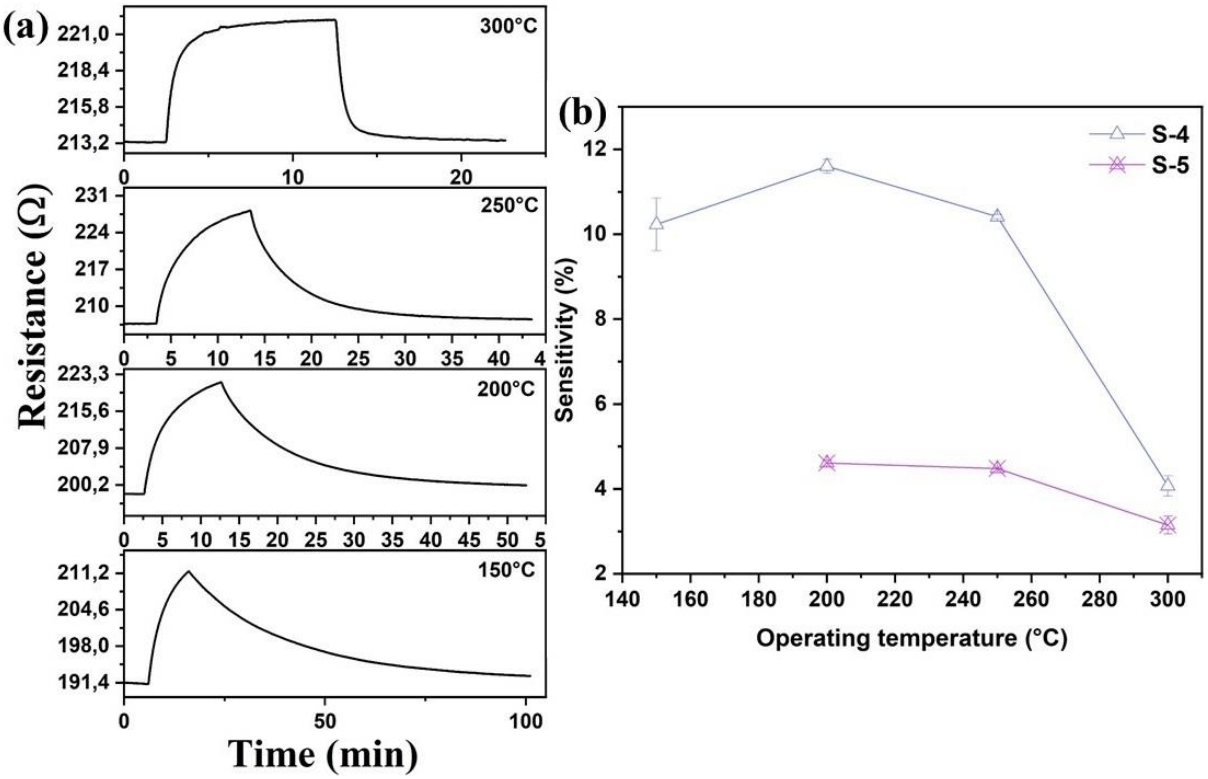


Figure 25 - (a) Dynamic response-recovery curves of S-4 towards 650 ppb $O_3$ and (b) sensitivities of S-4 and S-5 to 650 ppb $O_3$ at different working temperatures. S-4 (rGO/Ar+$O_2$) and S-5 (rGO/Ar+$O_2$).
Source: By the author

According to the results mentioned before, obtaining the best response regarding $O_3$ relies on both operating temperature and deposition parameters. On the one hand, ITO film deposited under pure Ar atmosphere and this same film deposited on rGO surface showed the highest responses to $O_3$ at high operating temperature. However, their response/recovery times were much prominent. On the other hand, Ar+$O_2$ atmosphere deposited ITO film on rGO surface showed, especially that of 100 nm thickness, the highest responses at low operating temperature, even though its response/recovery times became much larger as working temperature decreased.

Table 6 reports the sensing performances of our samples, ITO and rGO/ITO thin films, compared to other recent developments of sensing materials for ozone measurement. Even though these sensors do not work well at room temperature and, at the same time, have high sensitivity towards $O_3$, their sensitivity and the operating temperature are in accordance with the reported literature when RF magnetron sputtering technique was used. However, many efforts remain required to make these sensors present a high response to $O_3$.

Table 6 - Comparison of ozone sensing properties with different materials.

| Sensor | Synthesis method | $O_3$ (ppb) | Operating T, ºC | Sensor response ($R_{O3}$/Ra) | Ref. |
|---|---|---|---|---|---|
| **$WO_3$** | RF magnetron sputtering | 30, 400, 800 | 250 | 16, 263, 310 | 125 |
| **$WO_3$** | Thermal evaporation | 50, 175 | 300 | 1.25, 2.25 | 126 |
| **ZnO** | RF magnetron sputtering | 130 | 300 | 14 | 127 |
| **ZnO** | Chemical vapor deposition | 1000 | 440 | 1.8 | 128 |
| **rGO/ZnO** | RF magnetron sputtering | 100 | 300 | 49.6 | 120 |
| **$In_2O_3$** | RF magnetron sputtering | 85 | 200 | 1.10 | 85 |
| **CuO** | RF magnetron sputtering | 300 | 250 | 1.80 | 129 |
| **ITO** | RF magnetron sputtering | 2700 | 300 | ~1.18 | This work |
| **rGO/ITO** | RF magnetron sputtering | 650 | 200 | ~1.12 | This work |

Source: By the author

# 6 CONCLUSIONS

ITO and rGO/ITO thin films were successfully deposited by rf magnetron sputtering technique. Both ITO films and rGO/ITO samples exhibited, regardless of the different growth conditions, a single-phase diffraction pattern belonging to the cubic structure of $In_2O_3$. When the sample was deposited in a pure Ar atmosphere, in-situ thermal annealing led to larger grain sizes with two types of grain size distributions compared to ex-situ annealing processes. The use of $O_2$ during the deposition resulted in slightly larger grain sizes upon annealing. The rGO/ITO thin film deposited on Ar atmosphere turned out to be much more porous than the rGO/ITO deposited in a Ar+O2 atmosphere, since the oxygen content apparently has an inhibitory effect on the rGO surface.

Regarding the ozone sensing properties, we found that the sample annealed ex-situ at 300°C presented the best response to ozone compared with the ex- and in- situ annealing processes at 500°C and 200°C, respectively, which may be related to its small grain size and porosity. The sample annealed ex-situ at 300°C with 100 nm of thickness presents the better response to $O_3$ at a working temperature of 300°C. On the other hand, the ITO film deposited under Ar+O2 atmosphere showed shorter response and recovery times and a much lower response compared to the Ar-only deposited ITO sample. The combination of rGO with the Ar-film did not display a great difference on the gas response in relation to the Ar deposited film. On the other hand, the rGO/ITO film deposited on a $Ar+O_2$ atmosphere exhibited higher response for the whole $O_3$ concentrations in relation to the ITO film deposited in $Ar+O_2$ atmosphere, even though their sensitives were much lower than that the ITO and rGO/ITO films deposited on Ar atmosphere. Concerning the rGO/ITO samples, the rGO/ITO sample with 100 nm thickness and deposited on $Ar+O_2$ atmosphere showed a higher response to $O_3$ at a lower temperature. The response was roughly three times at 200°C compared with itself at 300°C.

## FUTURE PERSPECTIVES

- Verify the degree of selectivity of the films to other types of gases (CO, $NO_2$)
- Strategies to shorten both response and recovery times at lower operating temperatures

## REFERENCES


1 LUENGAS, A. *et al.* A review of indoor air treatment technologies. **Reviews in Environmental Science and Bio/Technology,** v. 14, p. 499–522 , 2015. DOI: 10.1007/s11157-015-9363-9.

2 WORLD HEALTH ORGANIZATION. **Urban health initiative***:* a model process for catalysing change: air pollution: effects on your body. Avalaible from: https://apps.who.int/iris/bitstream/handle/10665/340822/WHO-HEP-ECH-AQH-2021.2-eng.pdf?sequence=1. Accesible at: 20 June 2021.

3 LONG, R. W. *et al.* Comparison of ozone measurement methods in biomass burning smoke: an evaluation under field and laboratory conditions. **Atmospheric Measurement Techniques,** v. 14, n. 3, p. 1783–1800 , 2021.

4 WORLD HEALTH ORGANIZATION. **Ambient (outdoor) air quality and health**. Available from: http://www.who.int/mediacentre/factsheets/fs313/en/. Accesible at: 10 Feb. 2021.

5 SETT, D.; BASAK, D. Highly enhanced $H_2$ gas sensing characteristics of Co: ZnO nanorods and its mechanism. **Sensors and Actuators B:** chemical**,** v. 243, p. 475–483, 2017. DOI: 10.1016/j.snb.2016.11.163.

6 GONG, B. *et al.* UV irradiation-assisted ethanol detection operated by the gas sensor based on ZnO nanowires/optical fiber hybrid structure. **Sensors and Actuators B:** chemical**,** v. 245, p. 821–827, 2017. DOI:10.1016/J.SNB.2017.01.187.

7 RANA, L. *et al*. ZnO/ST-Quartz SAW resonator: an efficient $NO_2$ gas sensor. **Sensors and Actuators B:** chemical**,** v. 252, p. 840–845, 2017. DOI: 10.1016/j.snb.2017.06.075.

8 SUN, L. *et al*. Room-temperature CO thermoelectric gas sensor based on $Au/Co_3O_4$ catalyst tablet. **Nanotechnology**, v. 28, n. 7, p. 75501-75508, 2017.

9 MENART, E.; JOVANOVSKI, V.; HOČEVAR, S. B. Novel hydrazinium polyacrylate-based electrochemical gas sensor for formaldehyde. **Sensors and Actuators B:** chemical, v. 238, p. 71–75, 2017. DOI: 10.1016/j.snb.2016.07.042.

10 KONDO, T. *et al.* Room temperature ethanol sensor based on ZnO prepared via laser ablation in water. **Japanese Journal of Applied Physics**, v. 56, n. 8, p. 803041-8030143, 2017.

11 ZHANG, N. *et al*. Room-temperature high-sensitivity $H_2$ gas sensor based on dendritic ZnO nanostructures with macroscale in appearance. **Journal of Applied Physics,** v. 103, n. 10, p. 104305, 2008.

12 WETCHAKUN, K. *et al.* Semiconducting metal oxides as sensors for environmentally hazardous gases. **Sensors and Actuators B:** chemical, v. 160, n. 1, p. 580–591, 2011.

13 MIRZAEI, A. *et al.* Resistive gas sensors based on metal-oxide nanowires. **Journal of Applied Physics**, v. 126, n. 24, p. 241102, 2019.

14 KOROTCENKOV, G.; BRINZARI, V.; CHO, B. K. In2O3-and SnO2-based ozone sensors: design and characterization. **Critical Reviews in Solid State and Materials Sciences**, v. 43, n. 2, p. 83–132, 2018.

15 MALIK, R. *et al*. Functional gas sensing nanomaterials: a panoramic view. **Applied Physics Reviews**, v. 7, n. 21, p. 21301, 2020.

16 BHATI, V. S. *et al.* Improved sensitivity with low limit of detection of a hydrogen gas sensor based on rGO-loaded Ni-doped ZnO nanostructures. **ACS Applied Materials & Interfaces**, v. 10, n. 13, p. 11116–11124, 2018.

17 RI, J. *et al.* Sn-doping induced oxygen vacancies on the surface of the $In_2O_3$ nanofibers and their promoting effect on sensitive $NO_2$ detection at low temperature. **Sensors and Actuators B:** chemical**,** v. 317, n. 1-2, p. 128194, 2020.

18 MOKRUSHIN, A. S. *et al.* Pen plotter printing of ITO thin film as a highly CO sensitive component of a resistive gas sensor. **Talanta**, v. 221, p. 121455, 2021. DOI: 10.1016/j.talanta.2020.121455.

19 LEE, D.-J. *et al.* Highly selective ppb-level detection of $NH_3$ and $NO_2$ gas using patterned porous channels of ITO nanoparticles. **Sensors and Actuators B:** chemical, v. 216, p. 482–487, 2015. DOI: 10.1016/j.snb.2015.04.057.

20 XU, S.; SHI, Y. Low temperature high sensor response nano gas sensor using ITO nanofibers**. Sensors and Actuators B:** chemical, v. 143, n. 1, p. 71–75, 2009.

21 ZHU, X. *et al*. Enhancing the $NO_2$ gas sensing properties of rGO/$SnO_2$ nanocomposite films by using microporous substrates. **Sensors and Actuators B:** chemical, v. 248, p. 560–570, 2017. DOI: 10.1016/j.snb.2017.04.030

22 ANDRE, R. S. *et al*. Enhanced and selective ammonia detection using $In_2O_3$/reduced graphene oxide hybrid nanofibers. **Applied Surface Science**, v. 473, p. 133–140, 2019. DOI:10.1016/j.apsusc.2018.12.101.

23 DIETRICH, S. *et al.* Evaluation of indium tin oxide for gas sensing applications: adsorption/desorption and electrical conductivity studies on powders and thick films. **Sensors**, v. 21, n. 2, p. 497, 2021.

24 LIN, C.-W. *et al.* On an indium--tin-oxide thin film based ammonia gas sensor. **Sensors and Actuators B:** chemical, v 160, n. 1, p. 1481–1484 , 2011.

25 DING, Z. *et al.* Preparation of ITO nanoparticles by liquid phase coprecipitation method. **Journal of Nanomaterials**, v. 2010, p. 543601, 2010. DOI: 10.1155/2010/543601.

26 CHOI, J. H. *et al*. Design and characterization of Ga-doped indium tin oxide films for pixel electrode in liquid crystal display. **Thin Solid Films**, v. 527, p. 141–146, 2013. DOI:10.1016/j.tsf.2012.11.035.

27 AYDIN, E. B.; SEZGINTÜRK, M. K. Indium tin oxide (ITO): a promising material in biosensing technology. **TrAC Trends in Analytical Chemistry**, v. 97, p. 309–315, 2017. DOI: 10.1016/j.trac.2017.09.021.

28 KIM, J. W. *et al.* Fabrication of three-dimensional hybrid nanostructure-embedded ITO and its application as a transparent electrode for high-efficiency solution processable organic photovoltaic devices. **Nanoscale**, v. 9, n. 9, p. 3033–3039, 2017.

29 ZHAO, Q. *et al.* Printing of WO3/ITO nanocomposite electrochromic smart windows. **Solar Energy Materials and Solar Cells**, v 194, p. 95–102, 2019. DOI:10.1016/j.solmat.2019.02.002.

30 YILMAZ, P. *et al.* Spectrally selective PANI/ITO nanocomposite electrodes for energy-efficient dual band electrochromic windows. **ACS Applied Energy Materials**, v 3, p. 3779–3788, 2020. DOI:10.1021/acsaem.0c00241.

31 LI, H.-D. *et al.* Efficiency enhancement in polymer light-emitting diodes via embedded indium--tin--oxide nanorods. **ACS Applied Materials & Interfaces**, v. 7, n. 14, p. 7462–7465, 2015.

32 KUNDU, S.; KUMAR, A. Low concentration ammonia sensing performance of Pd incorporated indium tin oxide. **Journal of Alloys and Compounds**, v. 780, p. 245–255, 2019. DOI: 10.1016/j.jallcom.2018.11.201.

33 MAREZIO, M. Refinement of the crystal structure of $In_2O_3$ at two wavelengths. **Acta Crystallographica**, v. 20, n. 6, p. 723–728, 1966.

34 GALASSO, F. S. **Structure and properties of inorganic solids**. Oxford: Pergamon Press, 1970. (International series of monographs in solid state physics, v. 7).

35 NADAUD, N. *et al*. Structural studies of tin-doped indium oxide (ITO) and $In_4Sn_3O_{12}$. **Journal of Solid State Chemistry**, v. 135, n. 1, p. 140–148, 1998.

36 QIAO, Z. **Fabrication and study of ITO thin films prepared by magnetron sputtering**. 2003. 146 p. Dissertation (Doktor der Naturwissenschaften) - Fachbereich Physik, Universität Duisburg-Essen, Duisburg, 2003.

37 YAMADA, N. *et al.* Doping mechanisms of Sn in $In_2O_3$ powder studied using 119Sn Mössbauer spectroscopy and X-ray diffraction. **Japanese Journal of Applied Physics**, v. 38, n. 5, p. 2856–2862, 1999.

38 BEL HADJ TAHAR, R. *et al*. Tin doped indium oxide thin films: electrical properties. **Journal of Applied Physics**, v. 83, n. 5, p. 2631–2645, 1998.

39 GRANQVIST, C. G.; HULTÅKER, A. Transparent and conducting ITO films: new developments and applications. **Thin Solid Films**, v. 411, n. 1, p. 1–5, 2002.

40 GUILLÉN, C.; HERRERO, J. Influence of oxygen in the deposition and annealing atmosphere on the characteristics of ITO thin films prepared by sputtering at room temperature. **Vacuum**, v. 80, n. 6, p. 615–620, 2006.

41 LI, S.; QIAO, X.; CHEN, J. Effects of oxygen flow on the properties of indium tin oxide films. **Materials Chemistry and Physics**, v. 98, p. 144–147, 2006. DOI:10.1016/j.matchemphys.2005.09.012.

42 AMALATHAS, A.; ALKAISI, M. Effects of film thickness and sputtering power on properties of ITO thin films deposited by RF magnetron sputtering without oxygen. **Journal of Materials Science:** materials in electronics, v. 27, p. 11064–11071, 2016. DOI: 10.1007/s10854-016-5223-9.

43 YANG, C.-H. *et al*. The effect of annealing treatment on microstructure and properties of indium tin oxides films. **Materials Science and Engineering B**, v. 129, p. 154–160, 2006. DOI:10.1016/j.mseb.2006.01.012.

44 PARK, J; PARK, H. Optoelectric property and flexibility of tin-doped indium oxide (ITO) thin film. **Journal of Nanoscience and Nanotechnology**, v. 20, p. 3542–3546, 2020. DOI:10.1166/jnn.2020.17489.

45 KLEIN, E.; HUBER, K.; PAUL, O; RUTHER, P. Low-temperature plasma annealing of sputtered indium tin oxide for transparent and conductive thin-films on glass and polymer substrates. **Thin Solid Films**, v. 693, p. 137715, 2020. DOI:10.1016/j.tsf.2019.137715.

46 DONG, L. *et al.* Highly (4 0 0) preferential ITO thin film prepared by DC sputtering with excellent conductivity and infrared reflectivity. **Materials Letters**, v. 260, p. 126735, 2020. DOI: 10.1016/j.matlet.2019.126735.

47 BHORDE, A. *et al.* Room temperature synthesis of transparent and conducting indium tin oxide films with high mobility and figure of merit by RF-magnetron sputtering. **Journal of Electronic Materials**, v. 48, p. 7192–7202, 2019. DOI: 10.1007/s11664-019-07533-8.

48 ZHUO, Y. *et al.* Investigation on electrical properties of indium tin oxide thin films by effective control of crystallographic orientation. **Journal of Alloys and Compounds**, v. 786, p. 177–182, 2019. DOI: 10.1016/j.jallcom.2019.01.232.

49 NISHINAKA, H.; YOSHIMOTO, M. Mist chemical vapor deposition of single-phase metastable rhombohedral indium tin oxide epitaxial thin films with high electrical conductivity and transparency on various $\alpha$-$Al_2O_3$ substrates. **Crystal Growth & Design**, v. 18, p. 4022–4028, 2018. DOI: 10.1021/acs.cgd.8b00387.

50 DONG, L. *et al.* Preparation of indium tin oxide (ITO) thin film with (400) preferred orientation by sol--gel spin coating method. **Journal of Materials Science**: materials in electronics, v. 30, p. 8047–8054, 2019. DOI: 10.1007/s10854-019-01126-1.

51 THIRUMOORTHI, M.; PRAKASH, J. T. J. Structure, optical and electrical properties of indium tin oxide ultra thin films prepared by jet nebulizer spray pyrolysis technique. **Journal of Asian Ceramic Societies**, v. 4, p. 124–132, 2016. DOI:10.1016/j.jascer.2016.01.001.

52 HUANG, G. *et al*. Epitaxial indium tin oxide films deposited on yttrium stabilized zirconia substrate by DC magnetron sputtering. **Physica B:** condensed matter, v. 601, p. 412667, 2021. DOI: 10.1016/j.physb.2020.412667.

53 WU, W-F. *et al*. Effect of sputtering power on the structural and optical properties of RF magnetron sputtered ITO films. **Semiconductor Science and Technology**, v. 9, n. 6, p. 1242-1249, 1994.

54 JOHN, K. *et al*. In situ crystallization of highly conducting and transparent ITO thin films deposited by RF magnetron sputtering. **Vacuum**, v. 132, p. 91–94, 2016. DOI: 10.1016/j.vacuum.2016.07.035

55 KASHYOUT, A. *et al*. Studying the properties of RF-sputtered nanocrystalline tin-doped indium oxide. **International Journal of Photoenergy**, v. 2011, p. 1-6, 2011. DOI: 10.1155/2011/139374

56 ZHU, G.; YANG, Z. Effect of sputtering power and annealing temperature on the properties of indium tin oxide thin films prepared from radio frequency sputtering using powder target. **Journal of Materials Science:** materials in electronics, v 24, p. 3646–3651, 2013. DOI: 10.1007/s10854-013-1298-8.

57 LEBBAD, A. *et al.* Surface morphology, structural and electrical properties of RF-sputtered ITO thin films on Si substrates. **Bulletin of Materials Science**, v. 41, n. 3, p. 1–9, 2018.

58 MARIKKANNAN, M. *et al.* Effect of ambient combinations of argon, oxygen, and hydrogen on the properties of DC magnetron sputtered indium tin oxide films. **AIP Advances**, v. 5, n. 1, p. 17128, 2015.

59 WAN, D. *et al*. (211)-Orientation preference of transparent conducting In2O3: Sn films and its formation mechanism. **ACS Applied Materials & Interfaces**, v. 3, n. 12, p. 4751–4755, 2011.

60 HUANG, J.-L. *et al.* Investigation of reactive magnetron sputtering of indium tin oxide films on acrylics lattice parameters and stoichiometric compositions. **Journal of the Ceramic Society of Japan**, v. 108, n. 1253, p. 17–20, 2000.

61 WU, W.-F.; CHIOU, B.-S. Effect of oxygen concentration in the sputtering ambient on the microstructure, electrical and optical properties of radio-frequency magnetron-sputtered indium tin oxide films. **Semiconductor Science and Technology**, v. 11, n. 2, p. 196-202, 1996.

62 REDDY, V. S.; DAS, K.; DHAR, A.; RAY, S. K. The effect of substrate temperature on the properties of ITO thin films for OLED applications. **Semiconductor Science and Technology**, v. 21, n. 12, p. 1747–1752, 2006.

63 MALATHY, V. *et al.* Role of substrate temperature on the structural, optoelectronic and morphological properties of (400) oriented indium tin oxide thin films deposited using RF sputtering technique. **Journal of Materials Science:** materials in electronics, v. 21, p. 1299–1307, 2010. DOI:10.1007/S10854-010-0066-2

64 BINGYAN, R.; XIAOPING, L.; MINHUA, W.; YING, X. Preparation and characteristics of indium tin oxide (ITO) thin films at low temperature by rf magnetron sputtering. **Rare Metals**, v. 25, n. 6, p. 137–140, 2006.

65 YAMAMOTO, N.; MORISAWA, K.; MURAKAMI, J. ; NAKATANI, Y. Formation of ITO nanowires using conventional magnetron sputtering. **ECS Solid State Letters**, v. 3, n. 7, p. 84-86, 2014.

66 LI, Q. *et al.* Investigation of the influence of growth parameters on self-catalyzed ITO nanowires by high RF-power sputtering. **Nanotechnology**, v. 29, p. 165708, 2018. DOI: 10.1088/1361-6528/aaafa7.

67 MAJID, A.; KRUSPE, N. Hunter-gatherer olfaction is special. **Current Biology**, v. 28, n. 3, p. 409–413, 2018.

68 MAJHI, S. M. *et al.* Reduced graphene oxide (rGO)-loaded metal-oxide nanofiber gas sensors: an overview. **Sensors**, v. 21, n. 4, p. 1352, 2021.

69 GRABE, V.; SACHSE, S. Fundamental principles of the olfactory code. **Biosystems**, v. 164, p. 94–101, 2018. DOI: 10.1016/j.biosystems.2017.10.010.

70 KUMAR, A.; KIM, H.; HANCKE, G. P. Environmental monitoring systems: a review. **IEEE Sensors Journal**, v. 13, n. 4, p. 1329–1339, 2012.

71 DI NATALE, C. *et al.* Solid-state gas sensors for breath analysis: a review. **Analytica Chimica Acta**, v. 824, p. 1–17, 2014. DOI: 10.1016/j.aca.2014.03.014

72 PONZONI, A. *et al.* Nanostructured metal oxide gas sensors, a survey of applications carried out at sensor lab, Brescia (Italy) in the security and food quality fields. **Sensors**, v. 12,

n. 12, p. 17023–17045, 2012.

73 ZHANG, B.; GAO, P.-X. Metal oxide nanoarrays for chemical sensing: a review of fabrication methods, sensing modes, and their inter-correlations. **Frontiers in Materials**, v. 6, p. 1-20, 2019. DOI:10.3389/fmats.2019.00055.

74 DROBEK, M. *et al.* MOF-based membrane encapsulated ZnO nanowires for enhanced gas sensor selectivity. **ACS Applied Materials & Interfaces**, v. 8, n. 13, p. 8323–8328, 2016.

75 KIM, H.-J.; LEE, J.-H. Highly sensitive and selective gas sensors using p-type oxide semiconductors: overview. **Sensors and Actuators B:** chemical, v. 192, p. 607–627, 2014. DOI: 10.1016/j.snb.2013.11.005.

76 NAM, B.; KO, T.-K.; HYUN, S.-K.; LEE, C. CO sensing properties of chemiresistive $In_2O_3/SnO_2$ composite nanoparticle sensors. **Journal of Nanoscience and Nanotechnology**, v. 20, n. 7, p. 4344–4348, 2020.

77 GERASIMOV, G. N. *et al.* Structure and gas-sensing properties of $SnO_2$-$In_2O_3$ nanocomposites synthesized by impregnation method. **Sensors and Actuators B:** chemical, v. 320, p. 128406, 2020. DOI:10.1016/j.snb.2020.128406.

78 ZHOU, J. Y. *et al.* Gas sensing enhancing mechanism via doping-induced oxygen vacancies for gas sensors based on indium tin oxide nanotubes. **Sensors and Actuators B:** chemical, v. 265, p. 273–284, 2018. DOI:10.1016/j.snb.2018.03.008.

79 WANG, Q.; LIU, F.; LIN, J.; LU, G. Gas-sensing properties of In-Sn oxides composites synthesized by hydrothermal method. **Sensors and Actuators B:** chemical, v. 234, p. 130–136, 2016. DOI: 10.1016/j.snb.2016.04.042.

80 VAISHNAV, V. S.; PATEL, S. G.; PANCHAL, J. N. Development of ITO thin film sensor for detection of benzene. **Sensors and Actuators B:** chemical, v. 206, p. 381–388, 2015. DOI: 10.1016/j.snb.2014.07.037.

81 AFSHAR, M. *et al.* Indium-tin-oxide single-nanowire gas sensor fabricated via laser writing and subsequent etching. **Sensors and Actuators B:** chemical, v. 215, p. 525–535, 2015. DOI:10.1016/j.snb.2015.03.067

82 YAO, K.; TOOLE, R.; BASNET, P.; ZHAO, Y. Highly sensitive double-layered nanorod array gas sensors prepared by oblique angle deposition. **Applied Physics Letters**, v. 104, n. 7, p. 73110, 2014.

83 KOROTCENKOV, G.; CHO, B. K. Thin film $SnO_2$-based gas sensors: film thickness influence. **Sensors and Actuators B:** chemical, v. 142, n. 1, p. 321–330, 2009.

84 BARSAN, N.; SCHWEIZER-BERBERICH, M.; GÖPEL, W. Fundamental and practical aspects in the design of nanoscaled SnO2 gas sensors: a status report. **Fresenius' Journal of Analytical Chemistry**, v. 365, p. 287–304, 1999. DOI :10.1007/S002160051490

85 ATASHBAR, M. Z. Investigation on ozone-sensitive $In_2O_3$ thin films. **Thin Solid Films**, v. 354, n. 1-2, p. 222–226, 1999.

86 PANDYA, H. J.; CHANDRA, S.; VYAS, A. L. Fabrication and characterization of ethanol sensor based on RF sputtered ITO films. **Sensors & Transducers**, v. 10, p. 141-150, 2011. Available from: https://www.sensorsportal.com/HTML/DIGEST/february_2011/P_SI_139.pdf. Accessible at: 23 Jan. 2021.

87 ISIK, S. *et al*. Growth conditions effects on the $H_2$ and $CO_2$ gas sensing properties of indium tin oxide. **Journal of Physics:** conference series, v. 707, p.012021, 2016. DOI:10.1088/1742-6596/707/1/012021.

88 VASANTHIPILLAY, V.; VIJAYALAKSHMI, K. Effect of rf power on the structural properties of indium tin oxide thin film prepared for application in hydrogen gas sensor. **Journal of Materials Science:** materials in electronics, v. 24, n. 6, p. 1895–1899, 2013.

89 PILLAY, V. V.; GOYAL, S. Influence of sputtering power, annealing on the structural properties of ITO films, for application in ethanol gas sensor. **Materials Today:** proceedings, v. 2, n .9 p. 4609–4619, 2015.

90 VIJAYALAKSHMI, K. *et al*. Influence of deposition parameters and heat treatment on the $NO_2$ sensing properties of nanostructured indium tin oxide thin film. **Thin Solid Films**, v. 519, n. 10, p. 3378–3382, 2011.

91 LOU, X. *et al*. Gas-sensing properties of nanostructured $SnO_2$-based sensor synthesized with different methods. **Vacuum**, v. 81, n. 7, p. 883–889, 2007.

92 CANTALINI, C. *et al.* Investigation on the cross sensitivity of NO2 sensors based on $In_2O_3$ thin films prepared by sol-gel and vacuum thermal evaporation. **Thin Solid Films**, v. 350, n. 1-2, p. 276–282, 1999.

93 ZHANG, Y. *et al.* Gas-sensing properties of ITO materials with different morphologies prepared by sputtering. **SN Applied Sciences**, v. 2, n. 2, p. 1–11, 2020.

94 ZHANG, H. *et al*. $SnO_2$ nanoparticles-reduced graphene oxide nanocomposites for $NO_2$ sensing at low operating temperature. **Sensors and Actuators B:** chemical, v. 190, p. 472–478, 2014. DOI:10.1016/j.snb.2013.08.067.

95 NA, C. W. *et al.* Highly selective and sensitive detection of $NO_2$ using rGO-$In_2O_3$ structure on flexible substrate at low temperature. **Sensors and Actuators B:** chemical, v. 255, p. 1671–1679, 2018. DOI: 10.1016/j.snb.2017.08.172.

96 LIU, J. *et al.* Flower-like $In_2O_3$ modified by reduced graphene oxide sheets serving as a highly sensitive gas sensor for trace $NO_2$ detection. **Journal of Colloid and Interface Science**, v. 504, p. 206–213, 2017.DOI: 10.1016/j.jcis.2017.05.053.

97 NOGALES, C. G. *et al*. Ozone therapy in medicine and dentistry**. Journal of Contemporary Dental Practice**, v. 9, n. 4, p. 75–84, 2008.

98 PETRUCI, J. F. S. *et al.* Real-time monitoring of ozone in air using substrate-integrated hollow waveguide mid-infrared sensors. **Scientific Reports**, v. 3, n. 1, p. 3174, 2013.

99 ROCHA, L. S. R. *et al*. Novel ozone gas sensor based on ZnO nanostructures grown by the microwave-assisted hydrothermal route. **Ceramics International**, v. 42, n. 3, p. 4539–4545, 2016.

100 Yamazoe, N. *et al*. Interactions of tin oxide surface with $O_2$, $H_2O$ and $H_2$, **Surface Science**, v. 86, p .335-344, 1979. doi.org/10.1016/0039-6028(79)90411-4.

101 Sberveglieri, G. *et al.* Reactively sputtered indium tin oxide polycrystalline thin films as NO and NO2 gas sensors. **Thin solid films,** v. 186, n. 2, p. 349-360, 1990.

102 DEY, A. Semiconductor metal oxide gas sensors: a review. **Materials Science and**

**Engineering B**, v. 229, p. 206–217, 2018. DOI:10.1016/J.MSEB.2017.12.036.

103 WANG, C. *et al.* Metal oxide gas sensors: sensitivity and influencing factors. **Sensors**, v. 10, n. 3, p. 2088–2106, 2010.

104 TIEMANN, M. Porous metal oxides as gas sensors. **Chemistry:** a european journal**,** v. 13, n. 30, p. 8376–8388, 2007.

105 FINE, G. F.; CAVANAGH, L. M.; AFONJA, A.; BINIONS, R. Metal oxide semi-conductor gas sensors in environmental monitoring. **Sensors**, v. 10, n. 6, p. 5469–5502, 2010.

106 WILLIAMS, D. E. Semiconducting oxides as gas-sensitive resistors. **Sensors and Actuators B:** chemical, v. 57, n. 1-3, p. 1–16, 1999.

107 SHIMIZU Y. $SnO_2$ Gas Sensor. *In*: KREYSA G., OTA K., SAVINELL R.F. (ed.). **Encyclopedia of applied electrochemistry**. New York: Springer, 2014. DOI: 10.1007/978-1-4419-6996-5_475.

108 BARSAN, N.; WEIMAR, U. Conduction model of metal oxide gas sensors. **Journal of Electroceramics**, v. 7, n. 3, p. 143–167, 2001.

109 BARSAN, N.; KOZIEJ, D.; WEIMAR, U. Metal oxide-based gas sensor research: how to? **Sensors and Actuators B:** chemical, v. 121, n. 1, p. 18–35, 2007.

110 NAISBITT, S. C. *et al*. A microstructural model of semiconducting gas sensor response: The effects of sintering temperature on the response of chromium titanate (CTO) to carbon monoxide. **Sensors and Actuators B:** chemical, v. 114, n. 2, p. 969–977, 2006.

111 SHARMA, S.; MADOU, M. A new approach to gas sensing with nanotechnology. **Philosophical Transactions of the Royal Society A:** mathematical, physical and engineering sciences, v. 370, n. 1967, p. 2448–2473, 2012.

112 BOCHENKOV, V. E. *et al*. Sensitivity, selectivity, and stability of gas-sensitive metal-oxide nanostructures. 2010. Available from: http://www.chem.msu.ru/rus/books/2011/sergeev/all.pdf. Accessible at: 23 Jan. 2021.

113 JI, S.; YE, C. Synthesis, growth mechanism, and applications of zinc oxide nanomaterials. **Journal of Materials Science & Technology**, v. 24, n. 4, p. 1-16, 2008.

114 COLMENARES CALDERON, Y. **The effect of morphology and cobalt concentration on the sensing properties of zinc oxide sputtered films**, 2018. 80 p. Dissertation (Ciência e Engenharia de Materiais) - Escola de Engenharia de São Carlos, Universidade de São Paulo, São Carlos, 2018.

115 JACKSON, G. N. RF sputtering. **Thin Solid Films**, v. 5, n. 4, p. 209–246, 1970.

116 BOSCO, R. *et al*. Surface engineering for bone implants: a trend from passive to active surfaces. **Coatings**, v. 2, n. 4, p. 95–119, 2012.

117 HUMMERS JR, W. S.; OFFEMAN, R. E. Preparation of graphitic oxide. **Journal of the American Chemical Society**, v. 80, n. 6, p. 1339, 1958.

118 DE LIMA, B. S.; BERNARDI, M. I. B.; MASTELARO, V. R. Wavelength effect of ns-pulsed radiation on the reduction of graphene oxide. **Applied Surface Science**, v. 506, n. 11, p. 144808, 2020.

119 ARSHAK, K. *et al*. A review of gas sensors employed in electronic nose applications.

**Sensor Review**, v. 24, n. 2, p. 181–198, 2004.

120 DE LIMA, B. S. *et al.* Ozone detection in the ppt-level with rGO-ZnO based sensor. **Sensors and Actuators B:** chemical, v. 338, p. 129779, 2021. DOI:10.1016/j.snb.2021.129779

121 HU, Y. *et al*. Effects of heat treatment on properties of ITO films prepared by rf magnetron sputtering. **Vacuum**, v. 75, n. 2, p. 183–188, 2004.

122 DONLEY, C. *et al.* Characterization of Indium-Tin oxide interfaces using X-ray photoelectron spectroscopy and redox processes of a chemisorbed probe molecule: effect of surface pretreatment conditions. **Langmuir**, v. 18, n. 2, p. 450–457, 2002.

123 DANG, M. T.; LEFEBVRE, J.; WUEST, J. D. Recycling indium tin oxide (ITO) electrodes used in thin-film devices with adjacent hole-transport layers of metal oxides. **ACS Sustainable Chemistry & Engineering**, v. 3, n. 12, p. 3373–3381, 2015.

124 XING, R. *et al.* Preparation and gas sensing properties of $In_2O_3$/Au nanorods for detection of volatile organic compounds in exhaled breath. **Scientific Reports**, v. 5, p. 1–14, 2015. DOI: 10.1038/srep10717

125 BENDAHAN, M. et al. Characterization of ozone sensors based on $WO_3$ reactively sputtered films: influence of $O_2$ concentration in the sputtering gas, and working temperature. **Sensors and actuators B:** chemical, v. 100, n. 3, p. 320–324, 2004.

126 BITTENCOURT, C. *et al.* Effects of oxygen partial pressure and annealing temperature on the formation of sputtered tungsten oxide films. **Journal of the Electrochemical Society**, v. 149, n. 3, p. H81-H86, 2002.

127 COLMENARES, Y. N. *et al*. The effect of morphology on the ozone-gas sensing properties of zinc oxide sputtered films. **Thin Solid Films**, v. 703, p. 137975, 2020. DOI: 10.1016/j.tsf.2020.137975.

128 CHIEN, F. S.-S. *et al.* Fast-response ozone sensor with ZnO nanorods grown by chemical vapor deposition. **Sensors and Actuators B:** chemical, v. 144, n. 1, p. 120–125, 2010.

129 BEJAOUI, A. *et al*. Theoretical and experimental study of the response of CuO gas sensor under ozone. **Sensors and actuators B:** chemical, v. **1**90, p. 8–15, 2014. DOI:10.1016/j.snb.2013.06.084.

# ANNEX

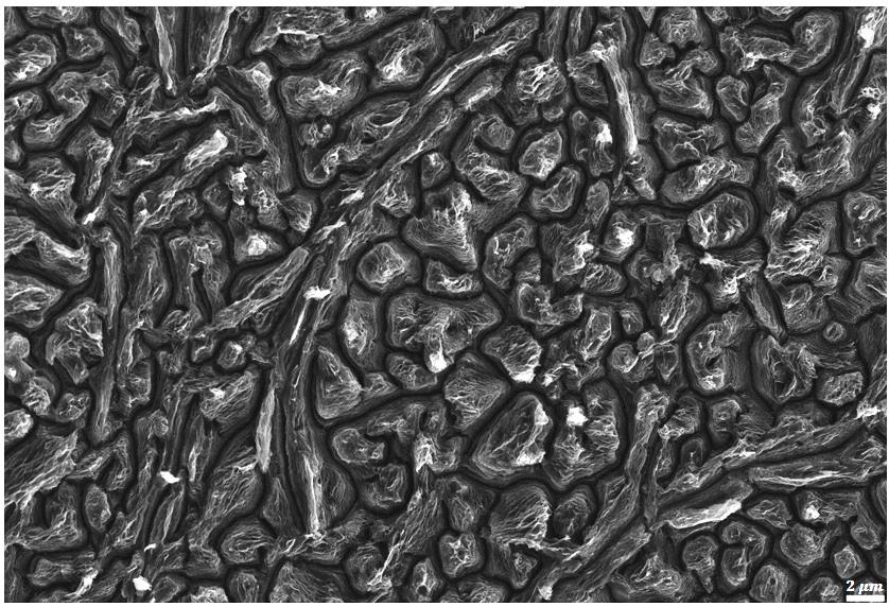


Figure A1 - SEM image of rGO with magnification of 5k.
Source: DE LIMA *et al.*[120]

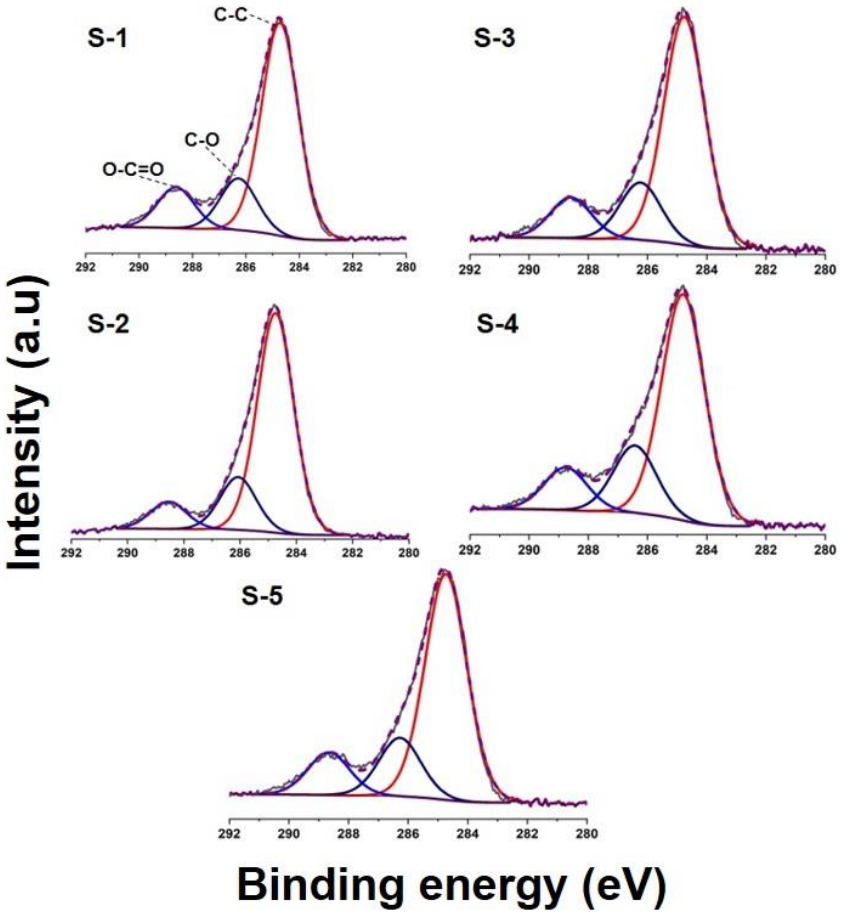


Figure A2 - High-resolution C 1s XPS spectrum of S-1, S-2, S-3, S-4 and S-5. S-1 (deposited under pure Ar atmosphere), S-2 (deposited under $Ar+O_2$ atmosphere), S-3 (rGO/Ar), S-4 (rGO/$Ar+O_2$) and S-5 (rGO/$Ar+O_2$).
Source: By the author

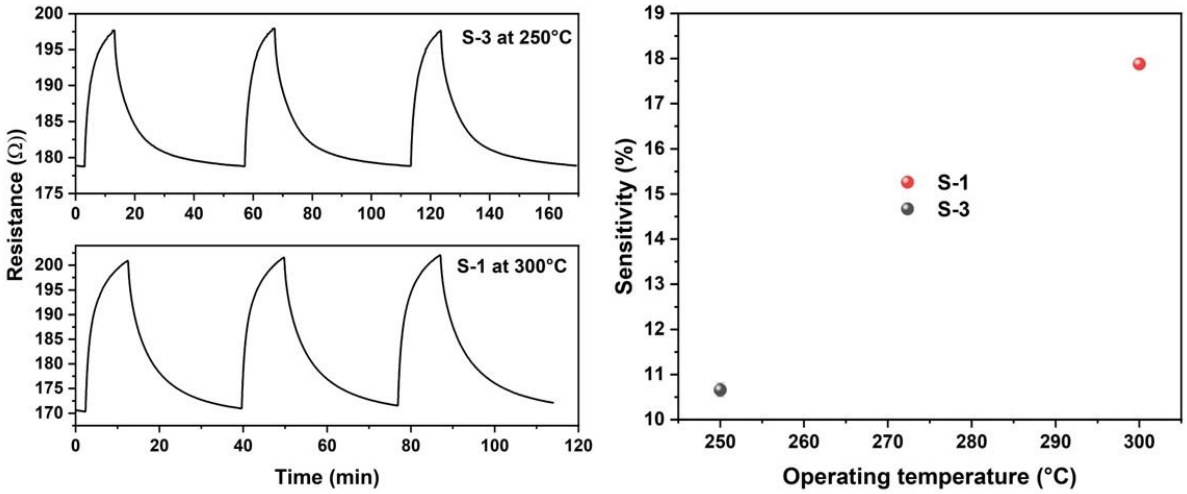


Figure A.3 - (left) Response curves and (right) sensitivities of S-1 and S-3 to 2.7 ppm $O_3$ at different working temperatures. S-1 (deposited under pure Ar atmosphere), S-3 (rGO/Ar).

Source: By the author